Focused Ion Beam Assisted Deposition of Gold

by

Gordon M. Shedd

B.S., Pennsylvania State University

(1984)

SUBMITTED IN PARTIAL FULFILLMENT
OF THE REQUIREMENTS OF THE DEGREE OF

MASTER OF SCIENCE
IN NUCLEAR ENGINEERING

at the
MASSACHUSETTS INSTITUTE OF TECHNOLOGY
September 1986

Signature of Author ______________________________
Department of Nuclear Engineering
August 8, 1986

Certified by ______________________________
John Melngailis
Thesis Advisor

Certified by ______________________________
Kenneth C. Russell
Thesis Reader

Accepted by ______________________________
Allan F. Henry
Chairman, Committee on Graduate Students

Focused Ion Beam Assisted Deposition of Gold

by

Gordon M. Shedd

Submitted to the Department of Nuclear Engineering
on August 8, 1986 in partial fulfillment of the
requirements for the Degree of Master of Science
in Nuclear Engineering

ABSTRACT

A focused beam of 15 keV Ga^+ ions was used to induce the selective chemical vapor deposition of gold films on silicon. Dimethylgold-hexafluoroacetylacetonate was directed toward the Si with a small tube, creating a localized pressure of .1–.4 mtorr. A submicron diameter ion beam was then scanned along the surface to induce the decomposition of adsorbed molecules. Gold lines of .75 microns in width were deposited by repeatedly scanning in one dimension. Yield was measured to be 4–5 gold atoms deposited per incident ion, when the ion dose per-scan was less than $10^{11}/cm^2$; higher doses produced lower yields. When the dose per-scan exceeded $10^{13}/cm^2$, etching of the Si occurred. Resistivity of the films was 200-500 times that of bulk gold. Auger analysis of the deposited material showed atomic concentrations of 75-80% Au, 15-20% Ga, and 5% or less of both carbon and oxygen.

Thesis Advisor:	John Melngailis
Title:	Principal Research Scientist Research Laboratory of Electronics

ACKNOWLEDGMENTS

The work described here could not have been performed without the assistance I received during every phase of the project. The focused ion beam, and the assistance required to make it work, came from IBS and its employees. Much use was made of the Submicron Structures Laboratory, the staff of which was unfailingly cooperative and patient. Resistivity measurements were made at Draper Laboratory, by Sam Smith, who was most unselfish with his time. Discussions with Prof. Carl Thompson helped to guide the interpretation of the observed resistivity. Additional thanks are due to Draper Laboratory for financial support of the project. For help with typing (and with simply surviving) during the manuscript preparation, I would like to thank my friend and partner, Suzanne Shedd. And finally, I want to thank the three people who have been most closely involved in this project. It has been a stimulating and pleasurable experience to work with Henri Lezec, whose early experiments laid the groundwork for this thesis, and with Andy Dubner, who will undoubtedly carry this process to fruition. The atmosphere within which we were able to cooperate so naturally was created for us by Dr. John Melngailis. For this, and for the direction and support he tendered throughout the course of the project, I am deeply grateful.

Contents

List of Figures

Chapter 1

Introduction

For most practical purposes, integrated circuits are small enough; they do not take up too much space, nor do they require excessive amounts of natural resources for their manufacture. However, the effort to shrink circuit dimensions still further has not abated. As long as increasing the number of circuit components on a chip can yield additional economic and performance advantages, the pursuit of smallness will continue.

A parallel effort is in progress to increase the number of components per chip not only by making devices smaller, but also by making the chips larger. Wafer scale integration entails placing many chip's worth of circuits into one huge circuit that spreads across an entire wafer. The complexity of the resulting circuit is a testimonial to computer-aided design, but it is sometimes easier to design something than it is to build it. As with the attempts to produce submicron circuit features, efforts to put wafer scale integration into practice are stretching the limits of processing capability.

1.1 Masking problems

Primary among the hindering factors encountered in attempts to make circuits smaller and more complex are limitations in the ability to define patterns in photoresist, the polymeric coating that is the staple of most lithographic techniques used for exposing part of the wafer surface for processing while protecting the rest. Two types of photoresist are used: positive resist, which becomes *less* soluble upon exposure to radiation, and negative resist, which becomes *more* soluble.

In a positive resist process, for example, a mask is placed above the coated wafer, allowing photons from a short wavelength source to impinge upon only those areas of photoresist underneath which the desired wafer processing is to be done. The wafer is then rinsed with a developer that dissolves the *exposed* photoresist, but leaves the rest intact.(Fig. 1.1)

The minimum feature size that can be reproduced by a lithographic technique depends, to a large extent, on the wavelength of the radiation source. Optical lithography, the most common tech-

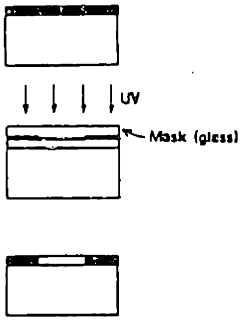

Figure 1.1: Steps in positive photoresist development. From Ref. [5]

nique, uses ultraviolet light, and can reliably reproduce features of about 1.5 μm. Lithographies based on x-rays, or deep ultraviolet radiation, can readily produce submicron features.

Whatever lithographic process is employed, the pattern reproduced on the wafer depends critically on the mask used—if there are defects in the mask, there will be defects on the wafer. Defects are defined relative to the minimum feature dimensions; a .2 μm radius bump on the edge of a 3 μm feature might not be considered a defect, but the same bump could become a defect if it were attached to a 1 μm feature [8].

Defects also become more problematic as the total area covered by a circuit increases. The product of defect density times the circuit area gives the number of defects per circuit, with .10 defects per circuit being equivalent to a 90% process yield. Therefore, as circuit area increases, defect density must decrease in order to maintain the same yield. When larger circuit area *and* smaller features are combined in the same circuit, it is an effectively hopeless task to make masks that do not include intolerable defects.

1.2 Solutions

1.2.1 Redundant circuit components

Two methods have been developed to deal with these defects. The first involves including redundant circuit components in the circuit design. Then, if a component is found to be defective, the metal stripes that connect it to the rest of the circuit can be severed by a laser beam. The connecting stripes that lead to the spare component are normally separated from the stripes of the main circuit by an insulating layer. At special sites on the wafer where the separated conductors intersect, the laser can be used to fuse them together, "wiring in" the replacement [13]. A disadvantage of this technique is that the sites required take up valuable space on the wafer.

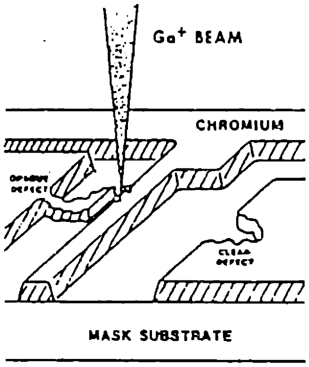

Figure 1.2: Illustration of opaque and clear defects. From Ref. [9]

1.2.2 Mask repair

The second method for overcoming defects is to eliminate them by repairing the mask itself. Masks are generally made by first depositing a metal layer on a transparent substrate. Subsequent steps define the mask pattern by etching away the metal where openings are desired. Mask defects occur when the etching eats into an area that should be covered, thereby creating a *clear* defect; or, when the etching fails to remove all of the metal from an opening, leaving behind an *opaque* defect. (Fig. 1.2)

Repairing opaque defects can be done with a short, high-powered laser pulse focused on the excess metal, a technique known as laser ablation. The pulse removes the defect by literally boiling the metal off of the surface. Another method for removing opaque defects is to mill them away using a finely focused beam of ions that have been accelerated to 15 keV or more. The focused ion beam (FIB), which can achieve a beam diameter of less than .1 μm, is capable of sputtering away defects with much greater precision than is possible with a laser.

Repairing clear defects is more difficut in that a small amount of material must somehow be *deposited* on the surface, rather than removed from it. Laser assisted chemical vapor deposition is one method by which metals can be deposited over small regions. The vapor of a metal compound is flowed over the surface while the laser irradiates the area where deposition is desired. Although lasers have been used successfully to induce the deposition of many metals, they are again limited in the mimimum area they can address. A combination of laser deposition followed by FIB milling has been used to repair small defects [10].

The FIB can be used to repair clear defects without laser deposition, as well. In fact, several companies market FIB systems specifically designed for repairing both opaque *and* clear defects. Two very different strategies are employed for clear defect repair. The first does not deposit material, but uses the precise milling ability of the FIB to create a light scattering structure on the surface of the transparent substrate. (Fig. 1.3) The second technique uses a process similar to the laser deposition, using the ion beam to

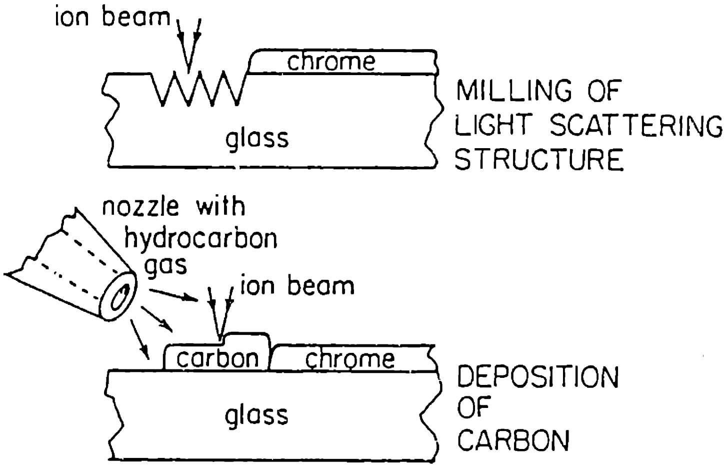

Figure 1.3: Repair of clear defects by milling and deposition.

induce the chemical vapor deposition of carbon at the defect site.

Both of these techniques are applicable to masks for optical lithography, but neither will work for x-ray mask repair. Of all lithography techniques, x-ray lithography appears to offer the most promise of providing submicron features at a high production rate [5]. But x-ray masks are very difficult to make defect-free, and, in fact, mask defects constitute *the* major stumbling block preventing the widespread adoption of x-ray lithography [8].

X-rays penetrate, so merely making a clear defect opaque is not enough—the material used for the mask must actually absorb the x-rays to prevent the underlying resist from being irradiated. Gold is almost always used, with a thickness of $\geq 0.5\ \mu m$ required to provide sufficient attenuation.

The requirement that clear defects be repaired by being filled in with an absorbing material has led to the development of techniques for the laser assisted deposition of gold. The aforementioned procedure combining laser deposition with FIB milling was specifically targeted for gold x-ray masks.

If the FIB could be used to assist gold deposition, then the entire mask repair routine could be performed using one machine. Earlier this year, it was suggested to this group that dimethy-gold-hexafluoro-acetyl acetonate (acac), a newly developed gold compound, might be a good candidate for an attempt at FIB-assisted deposition of gold.

An effort was already underway to use an FIB to induce the deposition of tungsten, aluminum, chrome, or some other conducting material. If successful, the goal was to use the material for the restructuring of integrated circuits—writing a line of metal from one conductor to another to connect them together. This procedure, when coupled with the FIB's ability to cut completely through a conductor, could be used to create intentional circuit faults (employed in the failure analysis of circuits), or to otherwise modify previously fabricated circuits.

Since attempts at depositing other metals had produced non-conducting oxide films, and, since gold is an excellent conductor that has no oxide form, it was decided to try to deposit gold from acac. The rest of this thesis concerns the work that has been done since that initial attempt, which yielded the first focused ion beam assisted deposition of gold.

Chapter 2

Equipment

2.1 The Focused Ion Beam

2.1.1 General description

A focused ion beam (FIB) is similar, in many respects, to a scanning electron microscope (SEM). In each, electric fields are used, first to extract particles from a needle-shaped source, then to accelerate and focus the particles into a fine beam having a diameter of 50 to 5,000 Å. Since the particles are charged, the beam can be deflected by electric fields oriented perpendicular to it, just as the electron beam in a cathode ray tube is rastered across the screen.

The primary difference between the two instruments, besides the obvious difference in particle type, is in the particle sources. In an SEM, a needle, usually tungsten, is brought close to a hole in a conducting surface. A potential difference, imposed between the needle and the surface, produces an electric field that is strongest at the needle's tip. There, electrons are emitted, swept up by the field, and accelerated toward the biased conductor. The hole, or extraction aperture, allows some of the electrons to pass through the conductor and into the focusing column.

In a FIB the ions come from a liquid source material that coats the needle rather than from the needle itself. The liquid, usually a metal, is supplied to the needle from a resistively heated reservoir. To do this when the source is operating at high voltages requires an electrically isolated current supply.

The source is kept at the electrical potential corresponding to the kinetic energy that the ions in the focused beam will possess. A metal plate, with a hole in its center, is mounted a fraction of a millimeter below the point of the needle. When the plate is maintained at a potential lower than that of the source, the difference (in most instances, 5–8 kilovolts) is the extraction potential. Under the influence of the high field induced by the extraction potential, the liquid at the needle's end is pulled into a sharp cone [11], the tip of which serves as a bright, point-like source of ions. (Fig. 2.1

It is the brightness and small size of the liquid metal ion source (LMIS) that make the high current density and small beam diameter of the FIB possible.

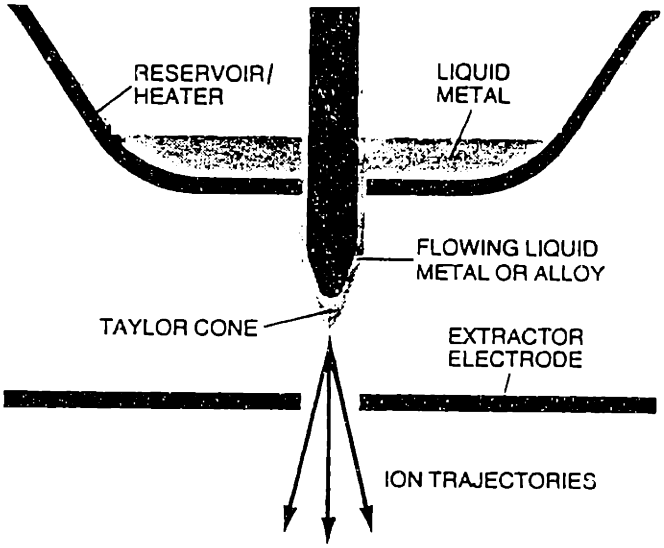

Figure 2.1: Liquid metal ion source. From Ref. [14]

Once the ions have been extracted from the source, they are accelerated toward the extraction plate by the 5–8 kilovolt potential drop. Ions that make it through the hole (aperture) in the plate, and a subsequent "beam-defining" aperture, are focused by a series of electrostatic lenses (Fig. 2.2), as well as being accelerated further as they fall to the zero of electrical potential. SEM images of beam traces milled in gold films indicate that ion beams of 300$\mathring{A}$ in diameter are achievable [25].

Before leaving the focusing column, the ions pass through a pair of fields which are oriented perpendicular to each other, and to the beam. These transverse fields can be varied electronically, allowing

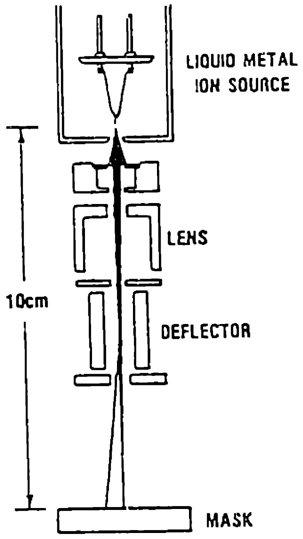

Figure 2.2: Focused ion beam column. From Ref. [10]

the beam to be steered, or scanned back and forth, depending on the input voltage signals.

2.1.2 The SIM-15

The FIB used for this work was a 15 kilovolt column manufactured in England by IBT-Dubilier. It was designed to be used as an ion microprobe for submicron resolution secondary ion mass spectroscopy (SIMS), a use for which a relatively modest accelerating potential is adequate. Since the minimum achievable beam diameter is inversely proportional to the ion energy [15], the SIM-15 beam is broader than those available in most other FIB's, which operate at potentials of up to 200 kilovolts.

The LMIS in the SIM-15 uses gallium, a particularly convenient metal since it has a melting point (303^0 K) that is just slightly above room temperature. In fact, the low melting point eliminated the need for an electrically isolated source heater current supply. After an initial period of heating, done using a conventional power supply, the heater coil could be disconnected, and the source elevated to its operating potential of 15 kilovolts. Several hours of operation could be realized with no additional heating. This was perhaps due to the heating effect of backstreaming secondary electrons [12] emitted from surfaces inside the column—the same potential drop that accelerates ions *away* from the tip, causes electrons to flow *toward* it.

2.2 Supporting components

2.2.1 Work chamber

The SIM-15 column is mounted to the top of a large cylindrical work chamber, designed by IBT for use with a 150 kilovolt FIB. Underneath the round chamber is a 2.5 inch thick steel table, supported by three pneumatic vibration-isolation legs. The work chamber is evacuated through a large exhaust port which feeds into a turbomolecular pump hanging below the table. (Fig. 2.3)

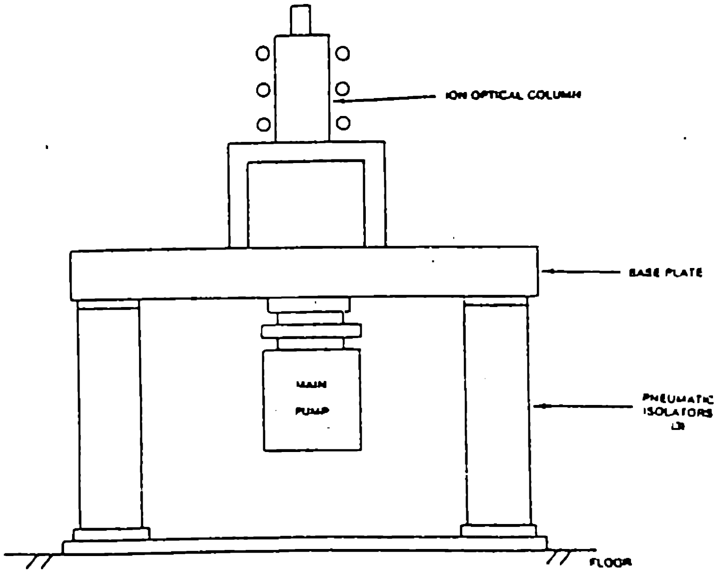

Figure 2.3: Schematic of FIB and supporting systems. From Ref. [16]

A sliding valve in the chamber wall separates the work chamber from an independently evacuated load lock, allowing a sample-holding cassette to be put in, or taken out of the work chamber without exposing the entire system to the atmosphere. The cassette slides on rails into a clamping mechanism mounted on top of an externally controllable X-Y translation stage. Once clamped to the stage, the sample holder can be moved under the protruding nose of the FIB.

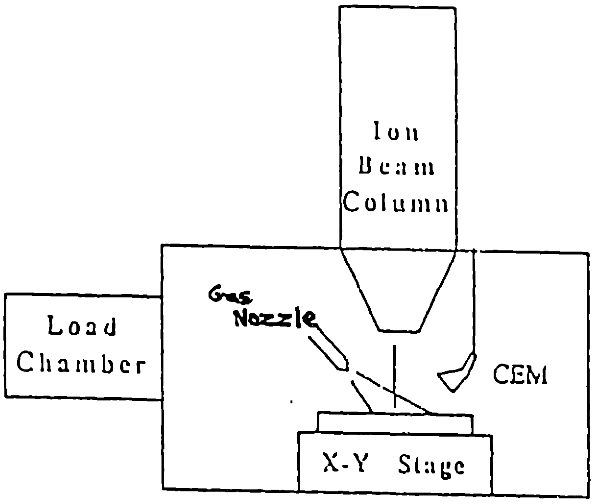

Figure 2.4: Interior of work chamber. From Ref. [14]

2.2.2 Secondary electron image and beam deflection

A channel electron multiplier (CEM) is positioned alongside the nose (Fig. 2.4), its open end angled down toward the sample to collect secondary electrons that are emitted when ions strike the surface. Each collected electron initiates a cascade of electrons in the multiplier, producing a macroscopic electrical signal that can be used to "see" the object that is being struck by the ions.

The ion beam can be scanned in synchronization with the rastering of the electron beam in an oscilloscope. By feeding the amplified secondary electron emission current into a circuit that modulates the intensity of the oscilloscope beam, an image of the surface is obtained.

The ratio of the size of the oscilloscope screen to the size of the area scanned by the FIB determines the magnification of the features observed. A maximum scan field of about 300 μm on a side is possible with the FIB system in its present configuration, yielding a *minimum* magnification of $\approx$ 175 X for an image viewed on a 5×5 cm. screen. Reducing the amplitude of the beam deflection signal reduces the size of the area scanned. With the SIM-15 column, surface features are still discernable when the scan field is cut to $5 \mu m$. on a side, giving a maximum *useful* magnification of $10,000\ X$.

The conventional video-rate deflection signal supplied with the SIM-15 was not ideally suited for experimental work. In particular, it did not allow the scan frequency to be varied. Provision was made, however, for controlling the deflection with an externally generated signal. Since the beam was scanned in only one direction during experiments, only one signal generator, capable of producing a variable-frequency sawtooth waveform, was needed.

2.2.3 Differential vacuum system

In general, particle beams are maintained in high-vacuum environments of 10^{-6} torr or *less*; low pressure CVD processes are carried out at gas pressures of 10^{-3} torr or *greater*. Satisfying both requirements simultaneously is achieved by differential pumping—the use of two separate vacuum systems. As mentioned previously, the work chamber is evacuated by a turbomolecular pump. The SIM-15 ion column used here has been modified to provide it with its own turbomolecular pump. Attached to the bottom of the ion column is a conical nose, open at the tip to allow the beam to exit. Since the beam is not deflected more than 200 μm from its axis, the nose hole can be reduced in size without causing interference.

A carbon diaphragm, with a .010 inch aperture is placed over the tip, then the column is aligned to center the beam in the aperture. The vacuum conductance of the aperture is small enough that a substantial pressure can be reached in the work chamber without excessively degrading the vacuum in the column.

The pressures in the work chamber and in the column were monitored with cold cathode vacuum gauges which registered down to a minimum of 10^{-7} torr. When no gas was being fed into the system both gauges were deflected below the 10^{-7} torr marks; however, cold cathode gauges are not necessarily accurate in this low pressure region. During experiments the work chamber pressure would rise to slightly above 10^{-6} torr, while the ion column gauge remained off scale.

2.3 Gas Feed System

Although most of the explication so far has concerned the machinery involved in supplying ions to the sample surface, the metal-bearing acac molecules are just as important to the deposition process. However, the system required to delilver the molecules is much less complicated.

At room temperature, acac is a liquid with a vapor pressure of only ≈ .7 torr. The low vapor pressure allows the gas source ampule to be connected directly to a stainless steel tube which terminates, inside the work chamber, with a 1.4 mm diameter nozzle that points at the area where the FIB impinges.

Figure 2.5 is a schematic diagram of the gas feed system, including the bypass tubing which is used to evacuate the line to the nozzle after experiments are completed. Dry nitrogen is used for line purging, and to speed up the pressure rise when the work chamber is vented.

The nozzle is located, vertically, below the nose of the FIB and about 1 mm above the sample surface. A set of two supporting arms, each attached to a micromanipulated stage, allows the nozzle to be precisely positioned in the horizontal plane. Positioning is simplified by the fact that the nozzle can be seen on the video monitor when the secondary electron image is observed. By plac-

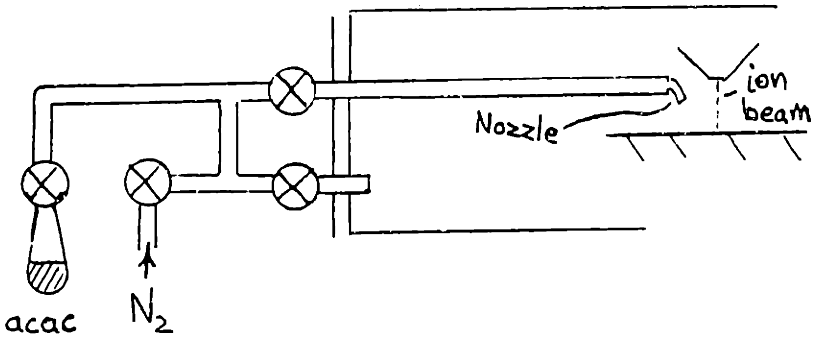

Figure 2.5: Schematic diagram of the gas feed system.

ing the nozzle in the same position for each experiment, pressure variation is minimized.

Chapter 3

Theory

3.1 Selective Chemical Vapor Deposition

The chemical vapor deposition (CVD) of a metal film results when molecules of a metal-bearing compound decompose, freeing the metal atoms to deposit on a surface. In most CVD processes, decomposition is induced by heating a substrate under an atmosphere containing the vapor of the compound. This usually yields a deposition that is nonselective— the entire substrate is coated with the metal film.

When the favorability of the reaction varies with position, deposition can become selective, "choosing" to occur in some areas and not in others. The ability to exercise precise control over the "choosing" is the primary attraction of focused ion beam assisted deposition.

In general, the CVD reactions of interest can be represented schematically by an equation of the following form:

$$A + MX_{vapor} \overset{\Delta E}{\Longrightarrow} M_{solid} + byproducts,$$

where MX is the compound containing the metal (M), A is another reactant species that may be required for the reaction to proceed, and ΔE is the net energy involved. The necessary reactants, *and* the necessary energetic situation must be present for deposition to take place.

Three basic strategies exist for predetermining which areas will be selected. They can best be illustrated by referring to the schematic equation given above.

1. Control over a reactant species other than the metal compound.

$$A(x) + MX_{vapor} \overset{\Delta E}{\Longrightarrow} M_{solid}(x) + byproducts,$$

Spatial control (indicated by (x)) over ancillary reactant species is usually exercised, directly,or indirectly, via control over the substrate composition. For example, atomic hydrogen is a necessary reactant for the deposition of tungsten from WF_6. Because molecular hydrogen does not readily decompose on SiO_2 surfaces, tungsten can be selectively deposited on silicon regions (where H_2 does decompose), while adjacent oxide areas remain untouched [6,1].

2. Control over the metal supply.

$$A + MX_{vapor}(x) \xRightarrow{\Delta E} M_{solid}(x) + byproducts,$$

Certain laser induced reactions rely on the creation of a highly localized plasma above the substrate. Decomposition of the molecules occurs in the gas phase, but the proximity of the substrate to the plasma causes the deposition to occur over a relatively small region [2,6].

3. Control over the energy supply.

$$A + MX_{vapor} \xRightarrow{\Delta E(x)} M_{solid}(x) + byproducts,$$

This is the most commonly used strategy for exercising precise control over depositions of minimum possible feature size. In this case, deposition occurs only where there is sufficient energy available to drive the reaction (the reactions are usually endothermic). The use of a focused beam of energetic particles (electrons or ions) [3,4], or photons, permits the transmission of energy to regions having dimensions comparable to the size of the beam itself (submicron). Lasers can provide a high power density, an advantage in terms of production capacity, but electron, and ion beams can be focused to much smaller diameters. In addition, charged particle beams can be deflected from point to point much more easily than can laser beams.

3.2 Ion beam/substrate interactions

3.2.1 Range of Ga^+ ions in Si and Au

In a beam of 15 keV Ga^+ ions incident on the surface of a solid, each ion will penetrate to a depth that is dependent on the rate at which the ion loses its kinetic energy to the atoms of the solid. The energy is exchanged through a series of collisions between the ion and the nuclei and electrons of atoms.

Each ion will have its own sequence of collisions which will lead it to stop at a particular depth, but when many ions are incident, the distribution of penetration depths can be described by the LSS[1] theory of projected range. Figure 3.1 shows the projected range (mean penetration depth) of arsenic ions into silicon as a function of initial kinetic energy. The projected range of Ga in Si should be almost the same as that of As, since, for a given substrate material, range is a function of the mass and nuclear charge of the ion. ($M_{Ga} = 70$, $M_{As} = 72$, $Z_{Ga} = 31$, $Z_{As} = 33$.) As the figure indicates, the mean penetration depth of 15 keV Ga ions into Si should be ~150 Å. The penetration depth of Ga ions into gold will be even less than 150 Å, since the nuclear stopping power of gold is about twice that of silicon [26].

---

[1] Linhard, Scharff, and Schiott

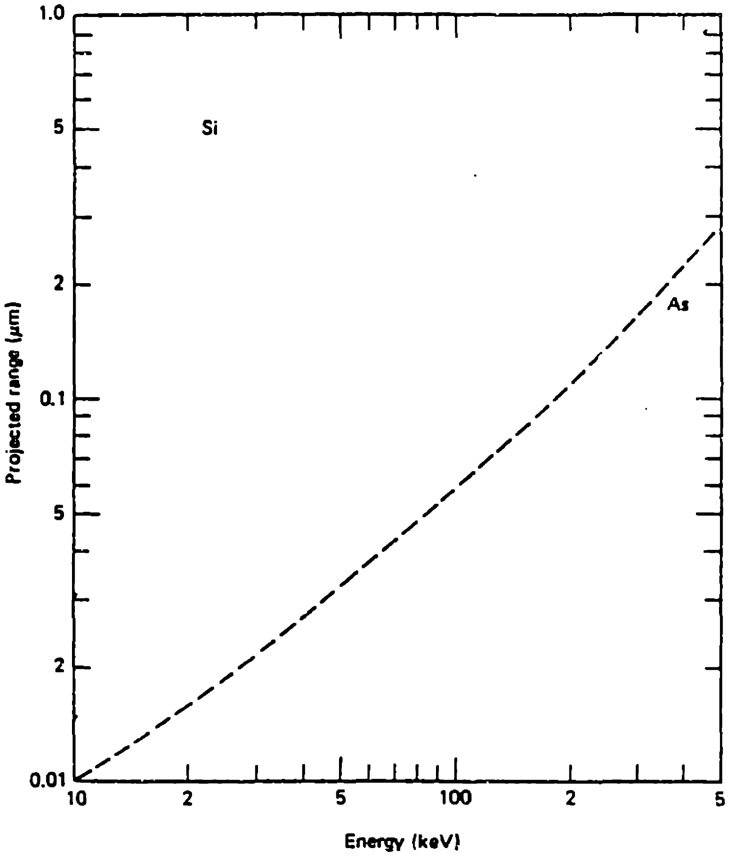

Figure 3.1: Projected range of arsenic in silicon. Adapted from [5].

3.2.2 Energy transfer mechanisms

The complete sequence of events by which the kinetic energy of an incoming ion is transformed into energy that drives a chemical reaction is not fully understood. At first glance, it might seem that the adsorbed gas molecules decompose upon being struck by the incident ions. However, as Rutherford showed with his gold films and α particles, most of the ions should pass through the first several layers they encounter without suffering a major collision. Any collision that did impart a significant portion of the ion's energy to a molecule would be likely to cause the molecule, or its fragments, to leave the surface.

Secondary electrons

As mentioned, the ion is brought to a stop by a series of collisions with electrons and nuclei. It is interactions with the free and bound electrons of the solid that produce the secondary electrons collected by the channel electron multiplier. These electrons have energies in the neighborhood of 10 eV, and some work with broad beams of low energy electrons has shown that they may cause chemical reactions to occur [21].

Thermal spikes

The energy of a 15 keV Ga^+ ion, incident on Si or Au, is transferred almost entirely to the nuclei, however [22]. The perturbed region surrounding an ion's path is on the order of 100 Åin diameter. Within this region, the energy transferred from the ion via nuclear collisions is thought to produce an effect similar to raising the temperature by several thousand degrees [23]. The "thermal spike" lasts only about 10^{-10} seconds [7], but that is more than long enough to affect a chemical reaction, as chemists' interest in sub-picosecond time-resolved-spectroscopy indicates.

Chapter 4

Preliminaries

4.1 The ion flux

In order to study the effect that a FIB has on a material or process, it is first necessary to establish a set of parameters that describes the beam. Although it is focused to an extremely small size, a FIB still has spatial extent, and within that extent there is variation in the beam's most elemental characteristic, the ion flux. In an ideal beam (one free of astigmatism), the variation in flux is modeled by a Gaussian distribution centered about the focal axis of the beam. How important the flux variation *is* in any particular instance will depend on the manner in which the beam is scanned.

4.1.1 The average flux: $\overline{\phi_i}$

When the SIM-15 is scanned over a two-dimensional field using a conventional video signal (256 lines, each scanned 60 times per second), the flux profile within the beam is of neglible import. After any reasonable period of time, the field will have received an essentially uniform dose of ions. The flux of interest in this case is the average flux ($\overline{\phi_i}$)— the number of ions per second coming down in the beam, divided by the area of the scanned field.

Presuming that the scanned area is known, $\overline{\phi_i}$is readily determined by measuring the electrical current carried by the positively charged ions in the beam. A picoammeter, inserted in series between a Faraday cup and electrical ground, can measure the beam current (i_b), a quantity that is directly proportional to the number of ions per second that are being directed toward the surface. The average ion flux is then given by $\overline{\phi_i} = i_b/qA$, A being the area impinged upon. Most of the experiments done here were at a beam current of 100 pA, while the scanned area was $\approx 250\ \mu\text{m}^2$, for an average ion flux of $\approx\ 2.5 \times 10^{14}\ \frac{\text{ions}}{\text{cm}^2-\text{sec}}$.

4.1.2 Ion flux profile

If the scanned pattern is changed from one involving many parallel lines to one in which only a single line is scanned, then the variation of the ion flux with position becomes more significant. The width of the beam's path will be equal to the diameter of the Gaussian profile. In addition, the magnitude of the flux will be greatest at the center of the path, tailing off towards the edges just as the profile does. For a beam centered at the origin, the ion flux is given by $\phi_i(r) = \phi_o \; exp^{\frac{-r^2}{2\Delta r^2}}$, where ϕ_o is the flux at $r = 0$, and Δr is the standard deviation of the Gaussian distribution.

Defining the beam radius is a matter of semantics, but it is conventional to equate it with Δr. At a distance Δr from the center of the beam, the flux has only decreased to 61% of its maximum value; furthermore, 61% of the ions in the beam fall outside a circle of radius Δr [24], *i.e.*

$$\frac{\int_0^{2\pi} \int_{\Delta r}^{\infty} \phi_i(r)\, r\, dr\, d\theta}{\int_0^{2\pi} \int_0^{\infty} \phi_i(r)\, r\, dr\, d\theta} = .61 \; .$$

However, when the beam is scanned along a line, it is only the beam profile in the direction transverse to the scan that is important; ions that fall 3 or 4 Δr in front of the beam axis still fall on the center of the line. This can be seen more easily by referring to Fig. 4.1, which shows graphically how the portion of the beam contributing to the flux within the line changes when the beam is scanned. Making use of the fact that $r^2 = x^2 + y^2$, coordinates of the Gaussian distribution can be changed from radial to Cartesian, allowing the percentage of the total ions falling more than Δr from

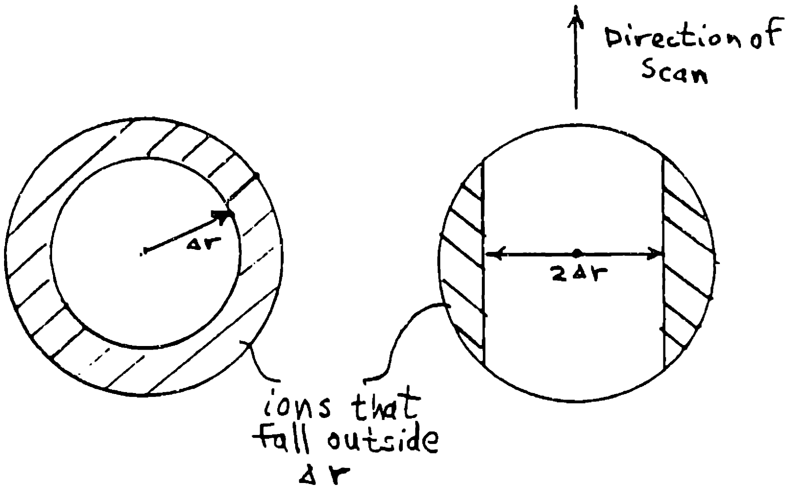

Figure 4.1: Area of interest changes when beam is scanned.

the center of the line to be calculated, *viz.*

$$\frac{\int_{-\infty}^{\infty} e^{\frac{-y^2}{2\Delta r^2}}\, dy \cdot 2\int_{\Delta r}^{\infty} \phi_o\, exp^{\frac{-x^2}{2\Delta r^2}} dx\, dx}{\int_{-\infty}^{\infty}\int_{-\infty}^{\infty} \phi_o\, exp^{\frac{-(x^2+y^2)}{2\Delta r^2}}\, dx\, dy} = .32$$

or 32%, a significant decrease from the 61% calculated for the stationary beam.

Since the ion beam in the SIM-15 was not sharply peaked, it was not easy to determine where its intensity had decreased to 61% of the maximum. It *was* possible to delineate the edge of the beam's path, and from this to estimate a beam diameter (d_b) that corresponded, most likely, to a distance of 4 Δr. At a radius of $\frac{d_b}{2} = 2\Delta r$, the flux has decreased to 14% of its maximum, and only 14% of the ions fall further away from the center. An average path was $\approx .8\ \mu$m wide, giving an estimate of $\Delta r \approx .2\ \mu$m. The maximum flux, ϕ_o, can be derived using this estimate of Δr and a measurement of the beam current.

4.1.3 Estimating the Maximum Flux, ϕ_o

It can be assumed that all of the ions in the beam are captured by the Faraday cup when the beam current is measured. This means that

$$2\pi \int_{-\infty}^{\infty} \phi_o \, r \; e^{\frac{-r^2}{2\Delta r^2}} \, dr = \frac{i_b}{q} \cdot$$

But the value of the integral is just $2\pi\Delta r^2$ times ϕ_o , so ϕ_o is determined to be

$$\phi_o = \frac{i_b}{q(2\pi\Delta r^2)} = \frac{8 i_b}{q(\pi d_b^2)} \cdot$$

From this, the total number of ions per second landing within a strip of width dx (Fig. 4.2), at the center of a line is given by

$$dx \int_{-\infty}^{\infty} \phi_o exp^{\frac{-y^2}{2\Delta r}} dy = \sqrt{2\pi}\Delta r \phi_o \, dx = \left(\frac{2\sqrt{2}}{\sqrt{\pi}}\right) \frac{i_b}{q d_b} dx \cdot$$

If the line has length L, then the flux along the center is the number per second, divided by the area impinged upon, or

$$\phi_i(x = 0) = \left(\frac{2\sqrt{2}}{\sqrt{\pi}}\right) \frac{i_b}{q d_b} \frac{dx}{L dx} = \left(\frac{2\sqrt{2}}{\sqrt{\pi}}\right) \frac{i_b}{q(d_b L)} \cdot$$

But d_bL is the area of the line, so, from the earlier definition of $\overline{\phi}_i$ as $\frac{i_b}{qA}$, the flux at the center of the line is

$$\phi_i(x = 0) = \frac{2\sqrt{2}}{\sqrt{\pi}} \overline{\phi}_i \cong 1.6 \overline{\phi}_i \cdot \tag{4.1}$$

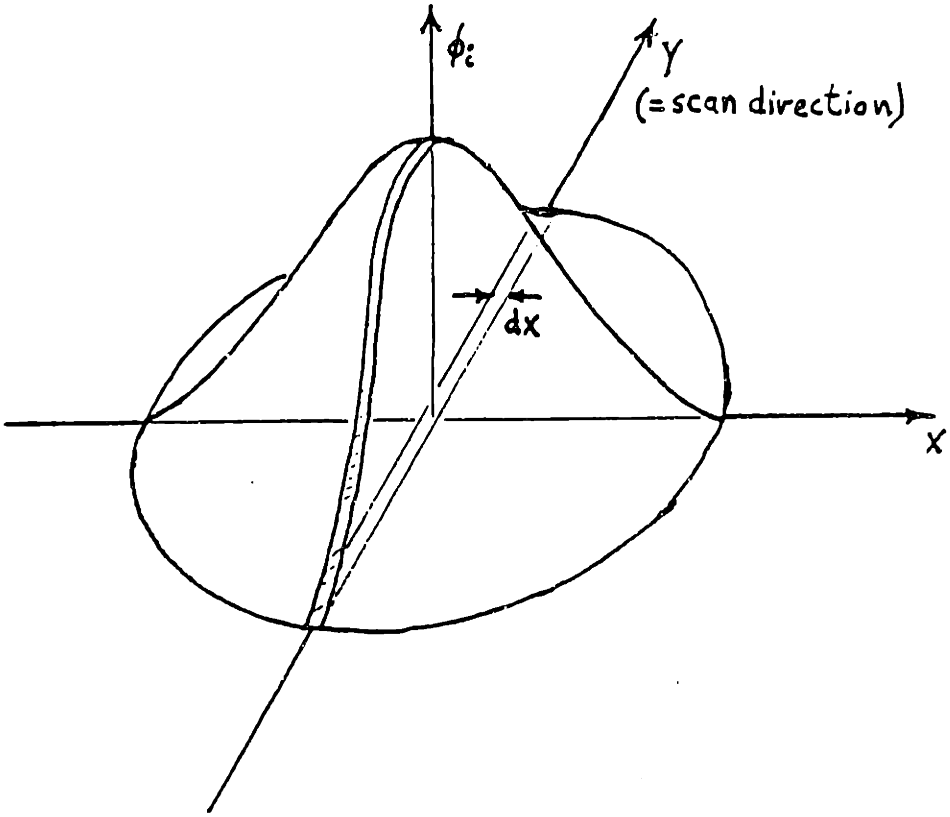

Figure 4.2: Representation of the dose per scan impinging on a point at the center of the line.

At $x = \Delta r$ the actual flux is almost identical to $\overline{\phi}_i$, so $\overline{\phi}_i$ can be considered to be a slightly low, but reasonable, estimate of the flux received within the most interesting portion of a scanned line.

4.1.4 Defining dose per scan, $\overline{\sigma}_i$

The total ion dose, $\overline{\Sigma}_i$, received by an area during an experiment is just the ion flux times the duration of the experiment in seconds; *i.e.*

$$\overline{\Sigma}_i \equiv \overline{\phi}_i \, t_{exp},$$

a number per cm^2. Whether the beam passes over the area once, or a million times during the experiment, $\overline{\Sigma}_i$ will be the same. However,the difference in the effect on the surface might be analogous to the difference between having 100 pounds of sand dropped on one's head a tablespoonful at a time, or all at once.

Consider a 1 μm × 250 μm line, being irradiated by an average ion flux of $2.5 \times 10^{14} \ \frac{\text{ions}}{\text{cm}^2\text{-sec}}$. During one second, each one μm long section of the line receives 2.5×10^6 ions. If the beam is scanned along the line only once every second, then all 2.5×10^6 ions impinge on the one μm^2 section during a four millisecond time period, followed by a 996 millisecond period when no ions arrive. In this instance, $\overline{\sigma}_i$ is $2.5 \times 10^6 \ \frac{\text{ions}}{\mu\text{m}^2}$. If the beam were scanned 1000 times per second, the dose per scan would be reduced a thousandfold, to $2.5 \times 10^3 \frac{\text{ions}}{\mu\text{m}^2}$. In general, $\overline{\sigma}_i$ as a function of scan length, beam diameter, beam current, and scan frequency, ν, is given as

$$\overline{\sigma}_i = \frac{\overline{\phi}_i}{\nu} = \frac{1}{\nu}\frac{i_b}{q(Ld_b)} \cdot \tag{4.2}$$

Of course, on an even more microscopic level, the dose per scan will vary across the width of the line, just as the ion flux varies. The actual dose per scan along the center of the line is (using the result of equation 4.1)

$$\sigma_i(x=0) = \frac{\phi_i(x=0)}{\nu} = 1.6 \cdot \left[\frac{1}{\nu}\frac{i_b}{q(Ld_b)}\right] \cdot \tag{4.3}$$

4.2 The Molecular Flux

Quantifying the flux of ions is relatively straightforward when compared to determining the flux of acac molecules to the deposition site. The molecules are neither electrically charged, nor confined to a focused beam, facts that make both the prediction and measurement of their behavior more complicated.

If the partial pressure of the acac vapor had been uniform throughout the work chamber, then a measurement of the pressure would have allowed the flux to be calculated, simply, from the kinetic theory of gases as:

$$\phi_m = \frac{P_{ac}}{\sqrt{2\pi mkT}} \tag{4.4}$$

where:

ϕ_m = the molecular flux

P_{ac} = partial pressure of acac in Pa

m = mass of the molecule

k = the Boltzmann constant

T = temperature in kelvin.

But the pressure is not uniform; the gas is flowing from a tube that is pointed toward the area where the ion beam strikes the sample.

An estimate of the molecular flux can still be made, however, by following the method of Ref. [17]. If the gas pressure at the mouth of the tube is low, then the particles issuing from the tube can be considered to travel in straight lines once clear of the tube. Here, a *low* pressure is one at which the mean free path of the molecules is greater than the distance to the surface.

If D is the distance from the tube along the tube's centerline, then the pressure at D is given as

$$P_{ac}(D) = P_{ac}(0)\left[1 - \frac{1}{\sqrt{1+\left(\frac{R}{D}\right)^2}}\right] \tag{4.5}$$

where R is the tube radius. (See Figure 4.3.)

The pressure at the tube mouth, $P_{ac}(0)$, can be determined if

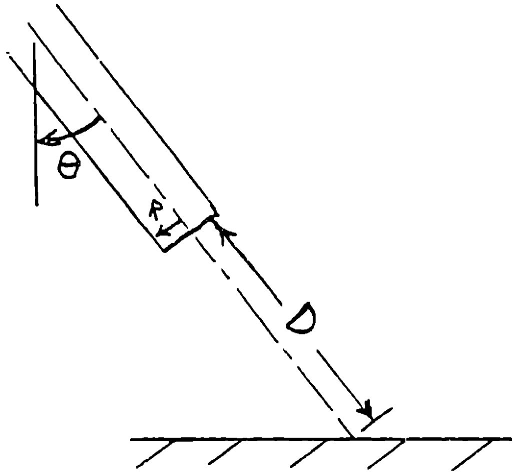

Figure 4.3: Nozzle coordinate system.

the flow rate of the gas through the tube is known [20], *i.e.*

$$P_{ac}(0) = \frac{\xi_{ac}}{\pi R^2}\left(\frac{1}{\overline{v}_{th}^{ac}}\right), \tag{4.6}$$

ξ_{ac} being the flow rate in $\left(\frac{\text{Pa-m}^3}{\text{sec}}\right)$, and $\overline{v}_{th}^{ac}$ is the thermal velocity of the gas, calculated from the kinetic theory of gases.

The flow rate of a gas through a tube can be calculated if the pressure drop across the tube, the dimensions of the tube, and the properties of the gas are known. If the gas is being fed into a vacuum chamber, then the pressure drop is essentially equal to the inlet pressure. The gas flow (at low pressure) is then described by [19]:

$$\xi_{(ac)} = \frac{1}{L}(2.904\overline{v}_{th}^{ac}R^3)\left[.0736\frac{RP_{ac}^2}{(\lambda P)_{ac}} + .81P_{ac}\right], \tag{4.7}$$

where L is the tube length, and λ is the mean free path of the gas.

Then, in terms of quantities that can be measured or calculated, the pressure at the intersection of the tube centerline with the surface, at a distance D from the tube, is

$$P_{ac}(D) = \frac{\xi_{ac}}{\pi R^2} \left(\frac{1}{\overline{v}_{th}^{ac}}\right) \left[1 - \frac{1}{\sqrt{1 + \left(\frac{R}{D}\right)^2}}\right] . \qquad (4.8)$$

A slight correction is needed to account for the angle of the tube with respect to the normal to the surface, but the change will not reduce the pressure by more than 30% for $\theta < 45^o$. Once this estimate of gas pressure at the surface is made, the molecular flux at the surface *can* be simply calculated, using equation 4.4, given at the beginning of this section.

Chapter 5

Experimental Procedures and Results

5.1 Measuring the Flow Rate of a Gas

As mentioned at the end of the previous chapter, it is necessary to measure the flow rate of acac through the nozzle in order to determine the flux of molecules to the surface where deposition occurs. The most convenient method for measuring ξ_{ac} would be to evacuate the work chamber, seal it off, and then feed the gas into the chamber while recording pressure as a function of time. This, coupled with a knowledge of the volume of the chamber, would yield the flow rate,*i.e.*

$$\xi = V \cdot \left(\frac{dP}{dt}\right),$$

where V is the work chamber volume. Unfortunately, the gauges used to read the work chamber pressure were calibrated to read pressures of nitrogen, not acac, so an alternative flow measurement procedure had to be devised.

It was decided to characterize the flow rate first by using nitrogen at an inlet pressure approximately equal to the vapor pressure of acac (.5-.7 torr). Using the method described above, it was found that , for an inlet pressure of .5 torr, the nitrogen flow rate was $\approx 3 \times 10^{-5}\left(\frac{\text{Pa-m}^3}{\text{sec}}\right)$.

If ξ_{N_2} is known, then ξ_{ac} can be estimated by making use of equation 4.7 in the following manner. For a given tube, and a given pressure drop, the ratio of ξ_{ac} under these conditions, to ξ_{N_2} for the same conditions, should be given as

$$\frac{\xi_{ac}}{\xi_{N_2}} = \left(\frac{\overline{v}_{th}^{ac}}{\overline{v}_{th}^{N_2}}\right) \frac{(\lambda P)_{N_2}}{(\lambda P)_{ac}} \left[\frac{.0736RP^2 + (\lambda P)_{ac}(.81P)}{.0736RP^2 + (\lambda P)_{N_2}(.81P)}\right] \equiv \mathcal{R}.$$

If $\mathcal{R}$ can be determined, then ξ_{ac} is simply

$$\xi_{ac} = \frac{\xi_{ac}}{\xi_{N_2}} \xi_{N_2} = \mathcal{R}\xi_{N_2}.$$

For a given gas, (λP) is approximately a constant [20], given by

$$(\lambda P)_i = \frac{kT}{\sqrt{2}\pi\delta_i^2},$$

where δ_i is the diameter of a molecule of species i. The thermal velocity of species i, with mass m_i, is given by

$$\overline{v}_{th}^{i} \equiv \sqrt{\frac{8kT}{\pi m_i}}.$$

If $\mathcal{L}$ is defined as

$$\mathcal{L} \equiv \frac{(\lambda P)_{N_2}}{(\lambda P)_{ac}} = \left(\frac{\delta_{ac}}{\delta_{N_2}}\right)^2,$$

and $\mathcal{M}$ is defined as

$$\mathcal{M} \equiv \frac{\overline{v}_{th}^{ac}}{\overline{v}_{th}^{N_2}} = \sqrt{\frac{m_{N_2}}{m_{ac}}},$$

then the flow rate of acac can be estimated to be

$$\xi_{ac} \approx [\mathcal{M}]\,[\mathcal{L}] \left[\frac{.0736RP^2 + \frac{1}{\mathcal{L}}(\lambda P)_{N_2}(.81P)}{.0736RP^2 + (\lambda P)_{N_2}(.81P)}\right] \xi_{N_2}.$$

For $\delta_{ac} \approx 12\AA$, $\delta_{N_2} = 3.7\AA$, and $\mathcal{M} = 3.94$, $\mathcal{R} \approx 1$, so the measured nitrogen flow rate can be used as an estimate of ξ_{ac} in equation 4.4. The radius of the nozzle was .685 mm, and the distance to the surface, D, was $\approx 2R$, so the pressure at the surface was estimated to be .1– 4 mtorr. At this pressure, equation 4.3 gives a molecular flux at the surface of $\approx\ 1 - 4 \times 10^{16}\ \frac{\text{molecules}}{\text{cm}^2-\text{sec}}$.

5.2 Etch-Deposition Transition

5.2.1 Initial Experiments

During the initial stages of the experimental work, the beam deflection electronics placed certain constraints on the range of possible experiments. The only signals available to scan the beam were the sawtooth waveforms used to produce a conventional, 256 lines/screen, ~60 screens/second, video monitor pattern.

If the vertical signal was disconnected, then a horizontal line could be scanned with 16 kHz analog x-scan signal. When the x-scan signal was disconnected, the 57.5 Hz digital y-scan signal would scan a vertical line. Reversing the leads also allowed the x signal to scan vertically, and the y signal horizontally.

5.2.2 Procedure

The first experiments involved writing vertical lines with the x-scan, and then the y-scan signals. While observing the secondary electron image on the monitor, the gas feed nozzle was brought into the field of view from the $-x$ direction, then centered vertically, and, finally, withdrawn to the $-x$ edge of the screen. The vertical orientation was chosen for line-writing to minimize the effect of the pressure drop that occurs on moving away from the nozzle.

Line length could be varied by adjusting the scan signal amplitude. A 40 volt peak-to-peak signal was chosen, which, it was later determined, gave a line length of 286 μm. To minimize horizontal beam deflection during the experiments, the cables that normally carried the x-scan signal were connected to each other, and to ground.

5.2.3 Initial Result

Although the scan generator could only supply the two fixed-frequency signals, the first bit of substantive information was revealed when the lines written with the two signals were observed—the 16 kHz signal caused deposition, but the 57.5 Hz signal caused etching. The digital raster of the low frequency signal was also apparent, as the etching occurred in a repeated, zipper-like pattern. (Fig. 5.1)

A signal generator was obtained, which allowed the frequency of the scan to be varied. To allow the scan frequency to be varied, a signal generator capable of producing sawtooth waveforms of adjustable duration was obtained. A set of experiments was performed in which the scan frequency was varied by factors of 10 from 0.4 Hz to 400 kHz. Scan length and beam current were the same in each experiment, 286 μm long, and 100 pA, respectively. The results showed that the 0.4 Hz signal produced etching, while deposition occurred at 40 Hz and above.

Although 40 Hz is a lower frequency than the 57.5 Hz at which etching had previously been observed, the beam current, and hence the ion flux, had been decreased by 50%. In addition, the 40 Hz signal was analog, so the beam was scanned smoothly along the line, rather than in the discrete, step-sit, step-sit, fashion that the digital 57.5 Hz signal produced.

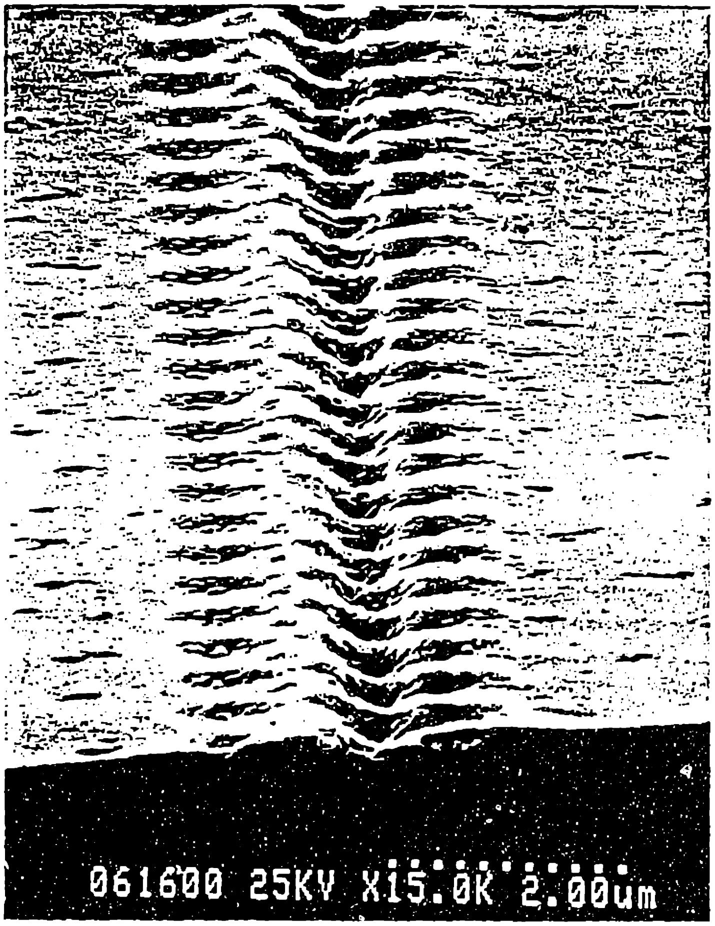

Figure 5.1: Etching produced by 57.5 Hz digital signal. 250 pA, 2400 sec., 286 μm length.

Digital *vs.* Analog

To confirm that the difference in beam motion could afect the results, a 57.5 Hz analog replica of the digital y-scan signal was generated. Using the same line length and beam current that had previously yielded the zipper-like etch pattern, another experiment was performed which resulted in deposition.

5.3 Dose per Scan Required to Induce Etching

When a 100 pA beam is scanned at 40 Hz over a 1 μm × 250 μm line, a 1 μm segment of the line receives 62,500 ions per scan. For this dose, deposition was observed. In an attempt to pinpoint the dose per scan at which the etch/deposition transition occurs, two series of experiments were performed. For each experiment, the dose per scan was predicted by assuming *a priori* that the line area would be 250 μm^2. Line length could be controlled by adjusting the scan signal amplitude, but line width varies from one experiment to the next. Since all of the experiments were viewed in an SEM to determine whether etching or deposition had occurred, it was a simple matter to measure linewidths *after* the experiments, and then to calculate more accurate values of dose per scan.

The first series of experiments used a 100 pA beam, and a 250

μm line length. The duration of the sawtooth ramp was varied from 31 msec (32 Hz) to 56 msec (18 Hz), which caused the corrected dose per scan to range from 75,000 to 134,000 $\frac{\text{ions}}{\mu\text{m}^2-\text{scan}}$. No etching of the silicon substrate was observed at any of these doses, but pronounced morphological variation was observed. As the dose per scan was increased, the texture of the deposited gold became increasingly globular (Fig. 5.2).

The second series of experiments used the same beam current, but the frequency was fixed at 40 Hz, and the linelength was varied. Decreasing the length of the line has the same effect on dose per scan that decreasing the frequency does. However, fixing the frequency assures that, at any point on the line, the time between irradiations will be the same. The molecules will have the same amount of time to be adsorbed in all of the experiments. Line length was varied from 416 μm down to 104 μm with resulting values of dose per scan of 50,000 to 200,000 $\frac{\text{ions}}{\mu\text{m}^2-\text{scan}}$. The etch/deposition transition observed in this case occurred between 100,000 and 150,000 $\frac{\text{ions}}{\mu\text{m}^2-\text{scan}}$. A later experiment, in which *deposition* was being attempted showed etching at 40,000 $\frac{\text{ions}}{\mu\text{m}^2-\text{scan}}$(Fig. 5.3).

Although the results were inconclusive, they indicate that the onset of etching occurs at a dose per scan in the neighborhood of 100,000 $\frac{\text{ions}}{\mu\text{m}^2-\text{scan}}$. Deposition was observed for doses up to

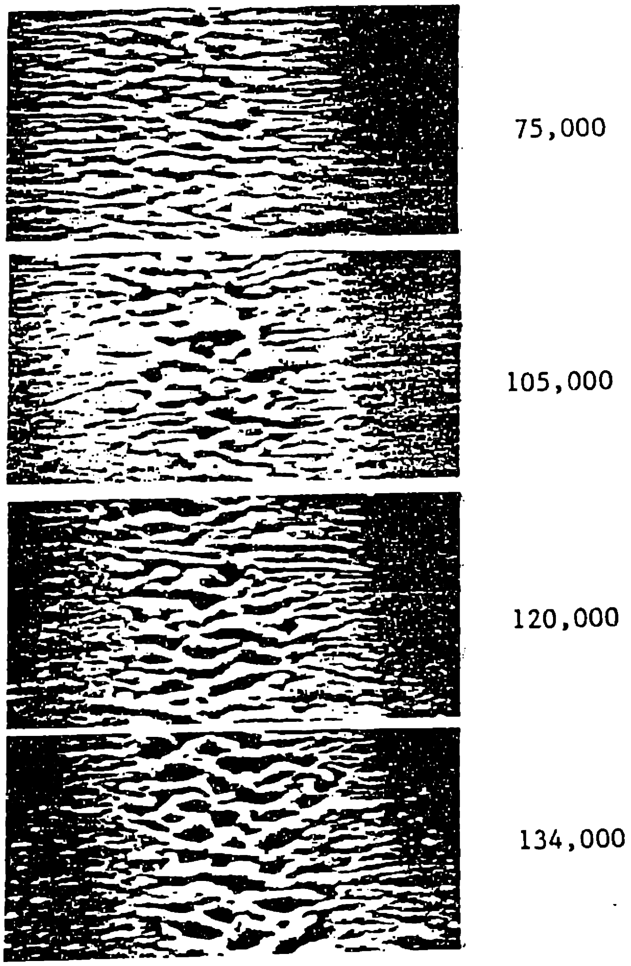

Figure 5.2: Texture change with increasing dose per scan ($\frac{\text{ions}}{\mu\text{m}^2-\text{scan}}$).

150,000 $\frac{\text{ions}}{\mu\text{m}^2-\text{scan}}$, and etching occurred after doses as low as 40,000 $\frac{\text{ions}}{\mu\text{m}^2-\text{scan}}$.

5.4 Deposition Yield

As the dose per scan is reduced to values lower than those that cause etching, deposition begins to occur. A series of experiments (mentioned in the previous section) had indicated that deposition occurs up to frequencies of at least 400 kHz, the limit imposed by the deflection electronics. To see if there is an optimum frequency for deposition, and to quantify the deposition rate, another set of experiments was performed.

5.4.1 Procedure

Sample preparation

For all of the experiments, the line length, beam current, and experiment duration were standardized at 250 μm, 100 pA, and 1000 seconds, respectively. Measuring deposition required that the deposited lines be cleaved in two, to be looked at end-on in an SEM. To assure that the $< 100 >$ silicon could be successfully broken directly beneath the 250 μm-long lines, the samples were pre-scribed along a cleavage direction. The samples were mounted on the sample-holder with the scribe marks parallel to the X−axis of the $X-Y$ stage. By watching the secondary electron image while moving the stage, a scribe mark could be located and aligned with the x−axis of the scan field. Vertically oriented lines were then deposited in the region just beyond the end of the scribe mark, as illustrated in figure 5.4.

Using this configuration it was possible to deposit up to ten parallel lines, then to cleave through all of the lines simultaneously, thereby assuring that the cross sections observed all came from approximately the same position in the lines. The number of samples that had to be mounted for viewing in the SEM was also greatly reduced by grouping the lines together.

Measurement of Deposition

To allow accurate measurement of the deposited lines, SEM photographs were taken of the view from above the sample, and of the head-on side view. The top view was used to measure line width. By tracing the outline of the deposited line onto semi-transparent graph paper, the cross sectional area could be measured. To minimize the error introduced by this measurement technique, all of the side view photographs were taken at the same magnification (40,000 X).

The volume of the deposited line was estimated by assuming a uniform cross section over the entire length of the line; when multiplied by the density of gold, the volume gave an estimate of the total number of gold atoms in the line. Dividing this number by the total number of ions that had impinged during the experiment gave the yield $\left[\frac{\text{Au atoms}}{\text{ion}}\right]$, a measure of the deposition efficiency.

Results

Gold lines were deposited at scan frequencies ranging from 40 Hz to 100 kHz. At the lower end of this range, deposition could barely overcome etching, and, as figure 5.3 in the previous section illustrates, the first few lines deposited did show the effects of etching.

Deposition yield is plotted in figure 5.5 as a function of dose per scan. The lowest point on the yield curve corresponds to the lowest frequency used, 40 Hz. Dose per scan was chosen as the ordinate because it reflects the effects of variations in frequency (ν) *and* linewidth (d_b), *i.e.* $\overline{\sigma_i} = \frac{1}{\nu}\frac{i_b}{q(Ld_b)}$.

As expected, when the dose per scan decreases, the etching decreases and the deposition yield increases. Yield continues to increase until $\overline{\sigma_i}$ is reduced to about $2 \times 10^{11}\ \frac{\text{ions}}{\text{cm}^2\text{-scan}}$. Looked at another way, $2 \times 10^{11}\ \frac{\text{ions}}{\text{cm}^2\text{-scan}}$ corresponds to a situation in which a 130Å radius circle on the surface receives one ion each time the beam is scanned. For a dose per scan of less than $2 \times 10^{11} \frac{\text{ions}}{\text{cm}^2-\text{scan}}$, deposition yield levels off at about 5 gold atoms deposited for each incident ion. Over a two order of magnitude span, deposition yield is essentially independent of $\overline{\sigma_i}$. Figure 5.6 shows a deposited line of ~ .75 μm in width, by .3 μm high; the Gaussian profile of the line is quite apparent.

5.4.2 Effect of Pressure on Yield

Over the course of the experimental work the liquid acac sources had to be replenished twice. Although there was still liquid present in the source ampule, the decreasing thickness of the deposited lines signalled the depletion of the acac supply. During a period shortly preceding one of these source changes, a set of experiments was done that reproduced the conditions of the set that produced the yield as a function of $\overline{\sigma_i}$ graph. The reproduced experiments did *not* reproduce the results. Instead, the yield was reduced to ~3 gold atoms/incident ion, as shown in figure 5.7. The previously observed flatness of the yield curve at low $\overline{\sigma_i}$ was again in evidence; the curve was merely displaced downward. The high $\overline{\sigma_i}$ experiments were not repeated, so the pressure dependence of the curve's break point was not determined.

5.5 Resistivity

Some of the proposed uses of FIB-assisted deposition would require a material that is an electrical conductor, so measurements were made of the resistivity of deposited gold lines. To allow contact to be made to the lines, metal contact pads were electron-beam evaporated on an insulating SiO_2 surface, as shown in figure 5.8. A gold line could then be deposited to form an electrical connection between the outer two pads. The inner two pads contact the line via thin "fingers". When a current is passed through the line from one outer pad to the other, the resistance of the line causes a voltage drop between the two fingers. The voltage drop is monitored with a voltmeter that has a much higher resistance than the line, so almost no current is shunted through the voltmeter. Knowing both the current passing through the line, and the voltage drop across it, the true resistance of the gold can be determined from Ohm's law. If the distance between the fingers (l), and the cross sectional area (A) of the line are measured, then the material parameter, resistivity, can be extracted from $R = \frac{\rho l}{A}$, where R is the measured resistance, and ρ is the resistivity.

The finger spacing was known, but the cross sectional area had to be determined for each line tested. To do this, the height of the line was measured with a Tencor α-step 200; the width was measured in the SEM. The area was calculated by assuming that the profile was a Gaussian, with a maximum value equal to the measured height, h, and a standard deviation, Δr, equal to one fourth of the line width (w). This gives:

$$area = \int_0^{2\Delta r} 2h\, exp^{\frac{-x^2}{2\Delta r^2}} dx = (.95)\,\frac{1}{2}\sqrt{\frac{\pi}{2}}\,(w \cdot h) \cong .6\,(w \cdot h).$$

The resistivities of the four lines measured ranged from 5×10^{-4} to 1.3×10^{-3} Ω-cm, considerably higher than the 2.2×10^{-6} Ω-cm of bulk gold.

5.6 Auger analysis of deposited film

To determine what impurities, if any, were present in the deposited gold, a sample was prepared for Auger analysis. Since analysis could not be performed on a line due to it small width, an 18 × 18 μm square was deposited. The elements looked for were those in the acac molecule (Au, C, O, and F), as well as Si and Ga. The results (although imprecise due to the standardized computer routine that established the atomic concentrations) showed the deposited film was about 75–80% gold, with the rest made up of 10–15% gallium, and about 5% each of carbon and oxygen. Figure 5.9 is a plot of atomic concentration as a function of sputter time, or depth into the sample. Unfortunately, carbon is not shown, but it was

less than 5%.

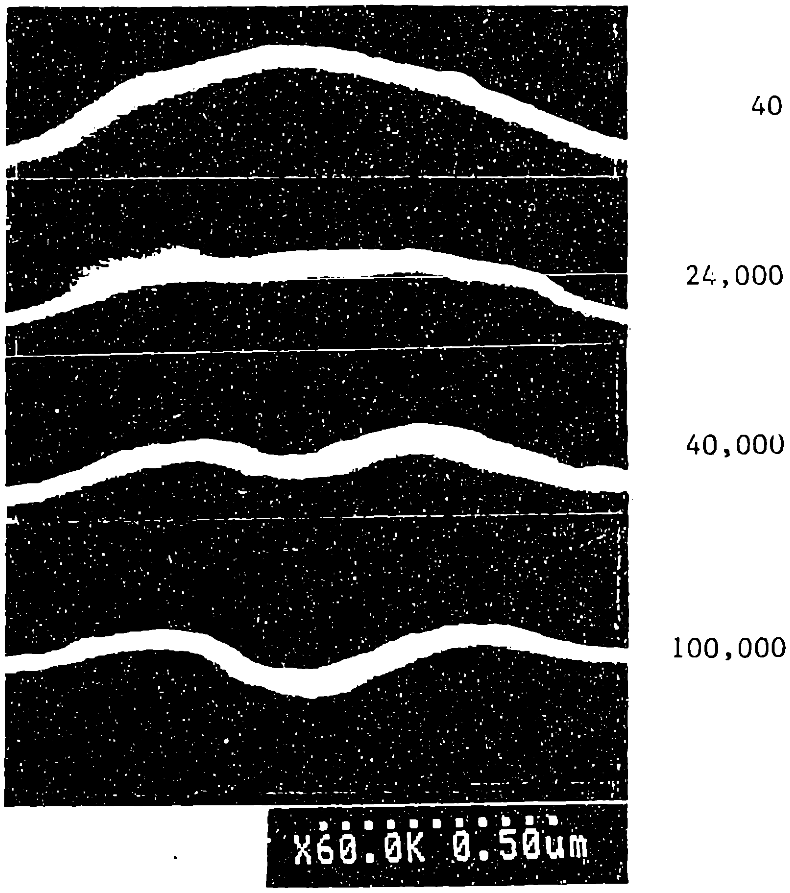

Figure 5.3: Etch/deposition transition with variation of ion dose per scan ($\frac{\text{ions}}{\mu\text{m}^2-\text{scan}}$).

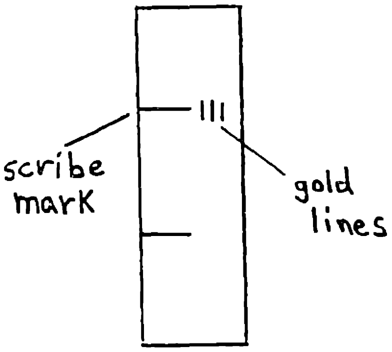

Figure 5.4: Sample arrangement.

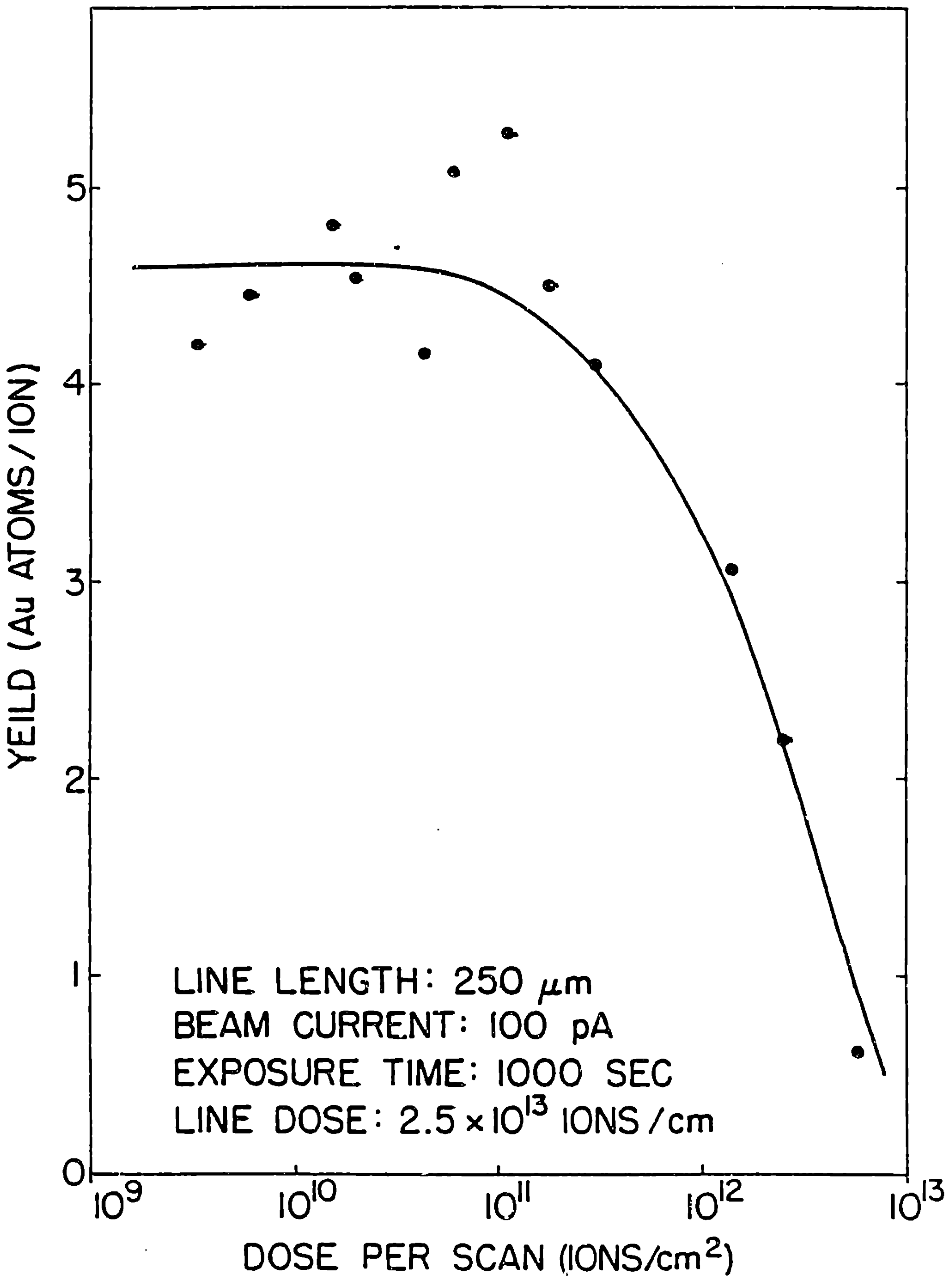

Figure 5.5: Effect of ion dose per scan on deposition yield.

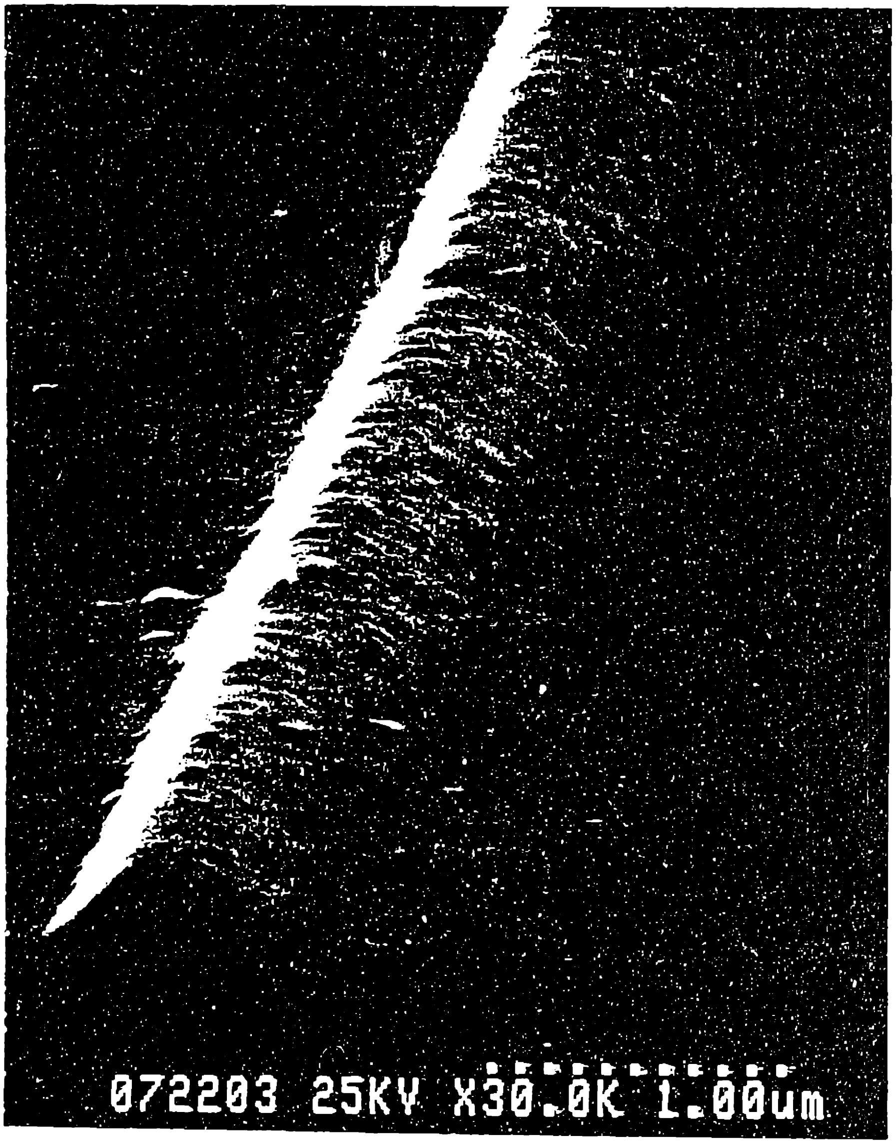

Figure 5.6: Focused ion beam assisted deposition of a submicron width gold stripe.

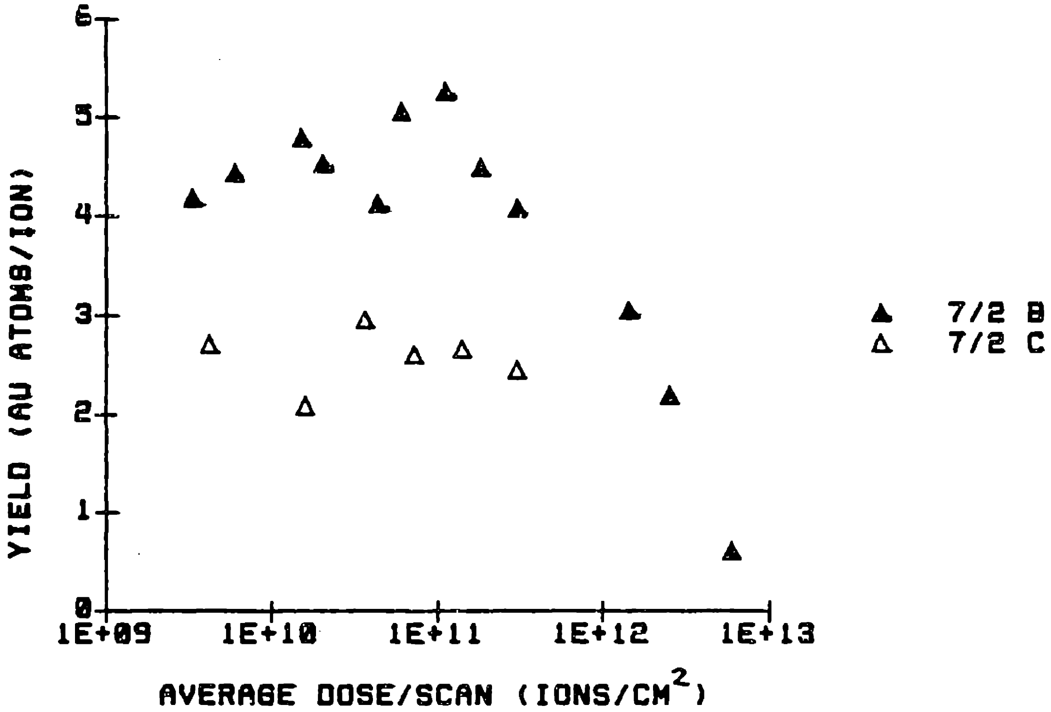

Figure 5.7: Effect of gas pressure on deposition yield.

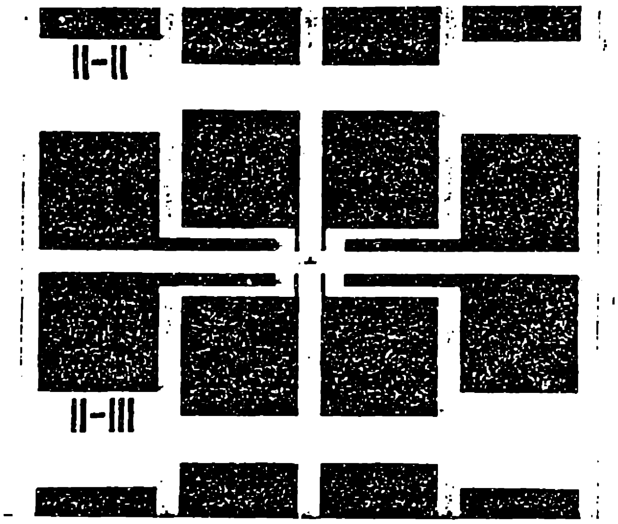

Figure 5.8: Contact pads for resistivity measurement.

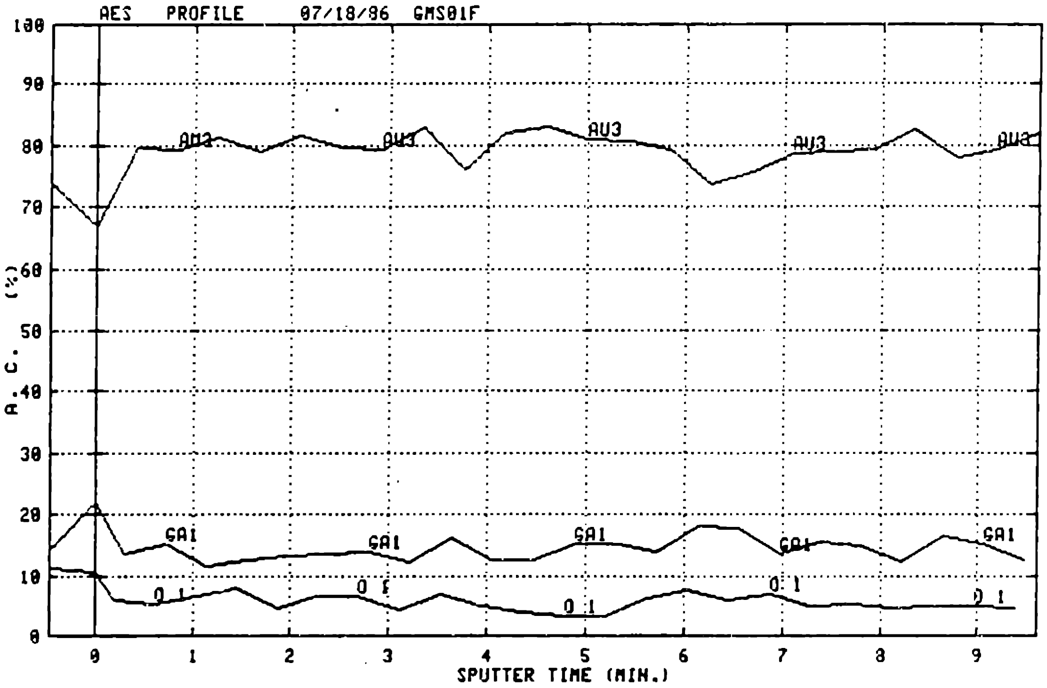

Figure 5.9: Atomic concentration as a function of sputter time (depth) for FIB-deposited gold film.

Chapter 6

Discussion

6.1 A Closer Look at Deposition

6.1.1 Surface concentration of molecules

To provide a framework within which FIB-assisted deposition can be understood, it is useful to have a simple picture of what is occurring at the sample surface. Two species are incident, each with its own characteristic impingement rate: ϕ_m for molecules, and ϕ_i for ions.

Some fraction of the molecules that hit the surface will be adsorbed; the others can be considered to be lost to the vacuum system. The fraction adsorbed is the sticking coefficient, χ_{st}. In the absence of any external agent to induce deposition, an adsorbed molecule will remain on the surface for some characteristic time, τ_d, before it desorbs.

For a given gas pressure, there will be some equilibrium surface concentration, σ_m^{eq}, for which the rates of adsorption and desorption are equal.

If the surface concentration is for some reason less than the equilibrium value, then the concentration will increase until the equilibrium concentration is reached. This build-up can be described mathematically as:

$$\frac{d\sigma_m}{dt} = \chi_{st}\phi_m - \frac{\sigma_m}{\tau_d},$$

where σ_m is the surface concentration of molecules $\left(\frac{number}{cm^2}\right)$.

In equilibrium, the rate of adsorption is equal to the rate of desorption, or

$$\frac{d\sigma_m}{dt} = \chi_{st}\phi_m - \frac{\sigma_m^{eq}}{\tau_d} = 0\,,$$

which, upon solving for σ_m^{eq} gives

$$\sigma_m^{eq} = \chi_{st}\phi_m\tau_d.$$

If σ_m^o is the concentration at $t = 0$, and τ_d is assumed to be independent of σ_m, then the two conditions, $\sigma_m(t = 0) = \sigma_m^o$, and $\sigma_m(t = \infty) = \sigma_m^{eq}$, allow the value of $\sigma_m(t)$ to be described as:

$$\sigma_m(t) = \sigma_m^o + \left(\sigma_m^{eq} - \sigma_m^o\right)\left(1 - e^{\frac{-t}{\tau_d}}\right), \qquad (6.1)$$

which is shown in Figure 6.1.

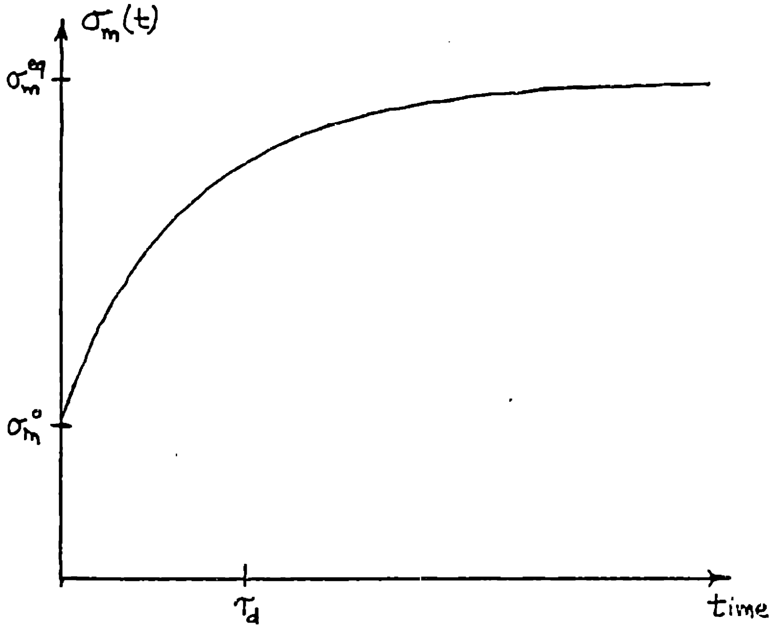

Figure 6.1: Time evolution of adsorbed molecule density.

6.1.2 Effect of Ions on Adsorbed Molecules

The introduction of the ion flux to the picture requires considering what effects an ion might have on the adsorbed molecules. Decomposition of the molecule, with the resultant deposition of a gold atom, is the desired effect, but the ion might cause molecules to desorb instead. Additionally, an ion could cause previously deposited gold atoms to be sputtered from the surface. Figure 6.2 illustrates the simple model that has been developed thus far.

To take the model a step closer to reality, the ion flux must be treated in more detail. During an experiment the FIB is scanned back and forth along a line, so the ion flux at a fixed point is far

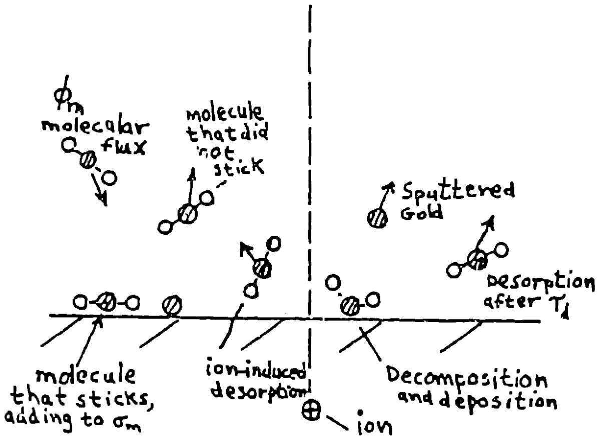

Figure 6.2: Schematic diagram of surface activities.

from constant. If the line is 250 μm long, then the beam is incident on a 1 μm long section of the line only .4% of the time. All of the deposition, ion-induced desorption, and gold sputtering that occurs within this segment of the line, occurs during a period that bears the same relationship to a full scan that Halley's comet bears to a human lifespan.

After the beam passes by, the concentration of molecules on the surface is lower than what it was before, and the situation returns to that of σ_m increasing towards its equilibrium value. The equation given earlier can still be used to describe $\sigma_m(t)$. but t is restricted to being less than the time it takes for the beam to come back again.

The graph in Figure 6.3 shows how σ_m will vary with time at a fixed point, if the time between exposures is equal to the period

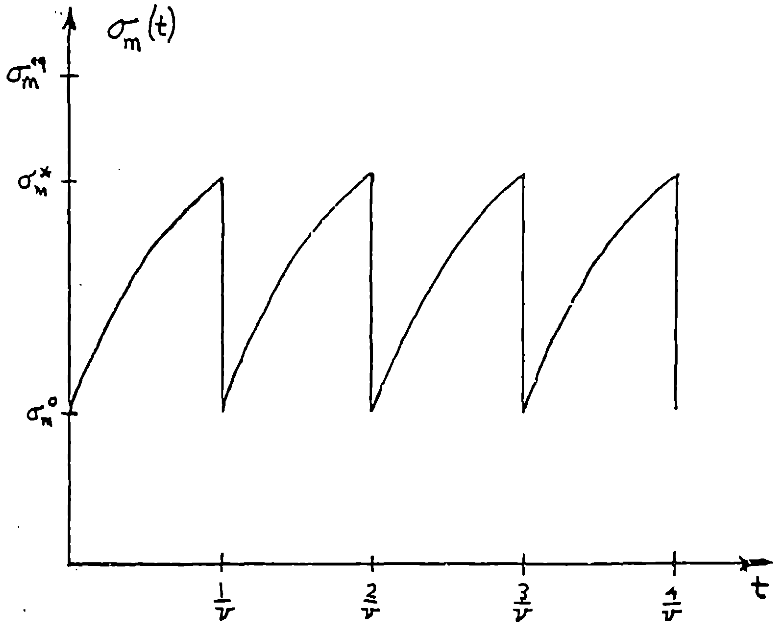

Figure 6.3: Adsorption with influence of ion beam.

of the scan (frequency^{-1}). The value of σ_m just before the beam arrives is σ_m^*, and σ_m falls to σ_m^o by the time the beam leaves. As the figure illustrates, the surface concentration of molecules will be the same each time the beam passes over a given point. As the beam moves to the next point on the line, it finds the same concentration of molecules waiting for it there, too. Every point that the beam approaches has had $(\frac{1}{\nu})$ seconds to recover from the previous visit. Using equation 6.1,σ_m^* can then be written as

$$\sigma_m^* = \sigma_m^o + (\sigma_m^{eq} - \sigma_m^o)\left(1 - e^{\frac{-1}{\nu\tau_d}}\right).$$

Decreasing the scan frequency should allow σ_m^* to increase, given the extra time for adsorption to occur, but if frequency is the only parameter changed, then the beam will remain longer at each point.

The surface concentration behind the beam, σ_m^o, will depend on the degree to which the adsorbed layer is depleted of molecules by the ion-induced desorption and deposition processes. Therefore, even if more adsorption occurs, there may be a net *decrease* inσ_m^*.

6.1.3 Transforming the situation to steady state

As was noted earlier, when the ion beam first impinges on a point, the concentration of molecules on the surface is σ_m^*. When the beam has finished passing over the point, the concentration is σ_m^o (which may well be zero). The flux of ions will also vary as the Gaussian flux distribution passes over the point. So during the period when deposition is occurring at a fixed point, σ_m and ϕ_i will both be changing constantly. Since deposition rate depends on both of these quantities, it too will change contantly.

The situation might be conceptually simpler if, instead of fixing the point, and having the beam pass by, perhaps the beam could be fixed, and the point could pass by. Establishing a coordinate system that moves along with the beam has the effect of fixing the beam's position. To an observer moving along with the beam, a side view of the beam/surface interface *will not change.* Figure 6.4 shows σ_m and ϕ_i as functions of position in a coordinate system moving with the beam. The two curves representing σ_m and ϕ_i do

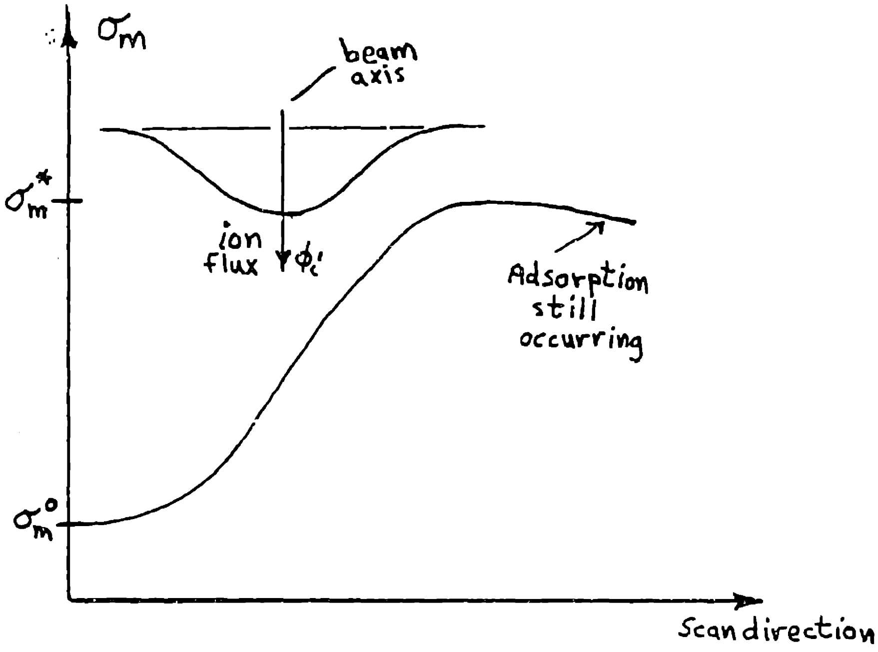

Figure 6.4: Surface concentration of adsorbed molecules as a function of position relative to the beam.

not move relative to each other. Therefore, at a fixed point in *this* coordinate system, σ_m, ϕ_i, and deposition rate will all be constant. This might be a useful way to look at FIB-assisted deposition when trying to model the processes that determine deposition rate.

6.2 Etching

As mentioned in chapter 5, etching was observed for $\overline{\sigma_i} = 40{,}000$ $\frac{\text{ions}}{\mu\text{m}^2\text{-scan}}$. The maximum dose, at the center of the line, is then (from equation 4.2) 64,000 $\frac{\text{ions}}{\mu\text{m}^2\text{-scan}}$. Deposition was observed for values

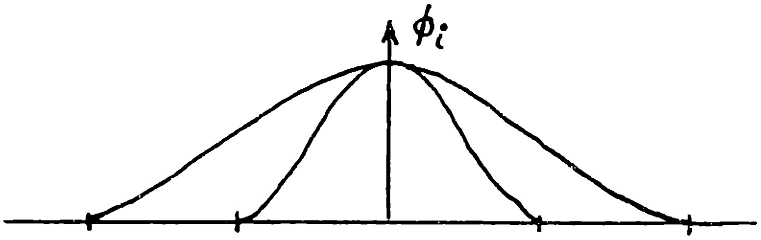

Figure 6.5: Dose per scan as a function of position for beams of different widths.

of $\overline{\sigma_i}$ greater than 100,000 $\frac{\text{ions}}{\mu\text{m}^2-\text{scan}}$, for which the maximum dose would be over 150,000 $\frac{\text{ions}}{\mu\text{m}^2-\text{scan}}$. Clearly it is not just the dose per scan that determines whether etching will occur; etching seems to be a function of beam diameter as well.

This can be explained by considering two lines, one scanned at 40 Hz, the other at 80 Hz. The first line receives twice as many ions per scan as the second line, but, if it is twice as wide as the second line, then the dose per scan will be the same for each line. Dose per scan as a function of position relative to the line center is shown in Figure 6.5.

The trenches etched in each case should to some extent mirror the curves shown; the dose per scan represented by the wider profile should etch a trench having gently sloping sides, whereas the narrower profile should produce a trench with steep sidewalls. If etching is purely a function of dose, then the trench depths should

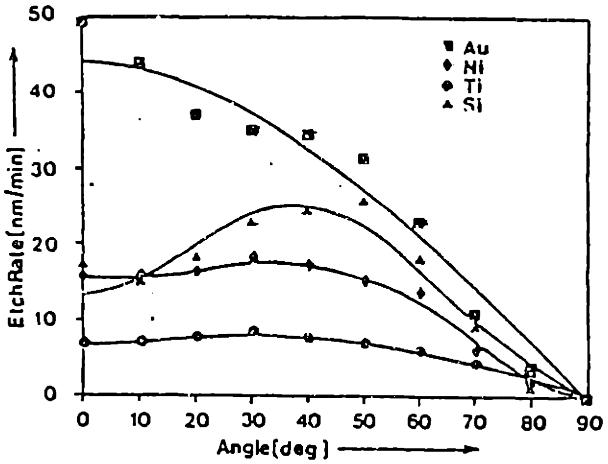

Figure 6.6: Etch rate as a function of angle of incidence.

be the same at the centers.

However, the geometry of the etched trenches has an impact on the magnitude of the etching. The steeper sidewalls produced by the narrow beam help to focus the impinging ions toward the center of the trench, thereby deepening it. In addition, silicon is sputtered more easily when ions are incident from an angle, as Figure 6.6 shows.

The ions that land in the wide trench approach at angles barely departing from normal to the surface, so their sputtering efficiency is lower than that of the ions that impinge on the angled surfaces in the narrow trench. When etching is competing with deposition, the narrow beam is more successful at keeping its trench from being filled in by the deposited material. It seems likely that narrower beams than the one used here will produce etching at even lower values of dose per scan.

6.3 Resistivity

The resistivity of the deposited gold was found to be 200-500 times that of bulk gold, and 10 times that of films deposited here using a broad beam of 750 eV argon ions. Several explanations for this are possible. If the grain structure of the films is such that voids are present, then the effective cross section through which the current can flow will be less than the measured cross section. If this is the cause of the problem, then conductivity might be improved by annealing the deposited material.

A second possibility is that gallium, or other impurities, may have a deleterious effect on conductivity. Gallium is unavoidable when it is used in the LMIS, as, once the film is more than about 200 Å thick, essentially all of the subsequent gallium ions are stopped by the gold.

The yield calculations, and Auger analysis, both showed a Au:Ga ratio of approximately 5:1, or 15-20 $^a/_o$. Figure 6.7 from [27] shows the resistivity of Au-Ga alloys as a function of atomic percent Ga. In the 15-20$^a/_o$ Ga range, resistivity is almost ten times that of pure gold, but this is a relatively minor increase compared to the

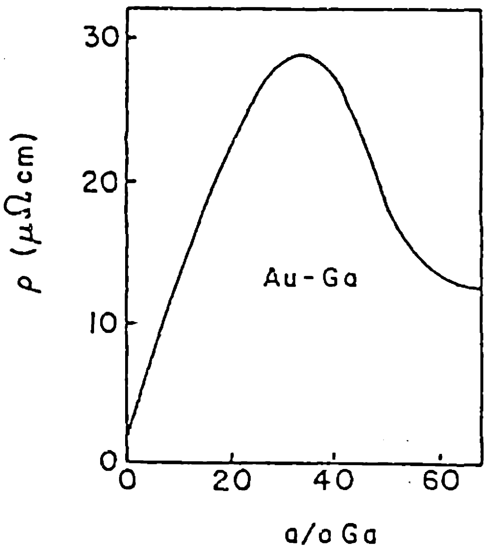

Figure 6.7: Resistivity of Au-Ga alloys. From [27].

observed resistivity.

A more significant problem that may ensue from the inclusion of gallium is a limitation on the range of possible annealing temperatures. As Figure 6.8 indicates, for temperatures above 415°C, Ga forms a liquid phase at the concentrations present here. Gallium is the most convenient material to use as an ion source, due to its low melting point, but for applications in which resistivity *must* be minimized, switching to a gold source would allow higher annealing temperatures to be used. In addition, any resistivity degradation due to the effects of alloying would be eliminated.

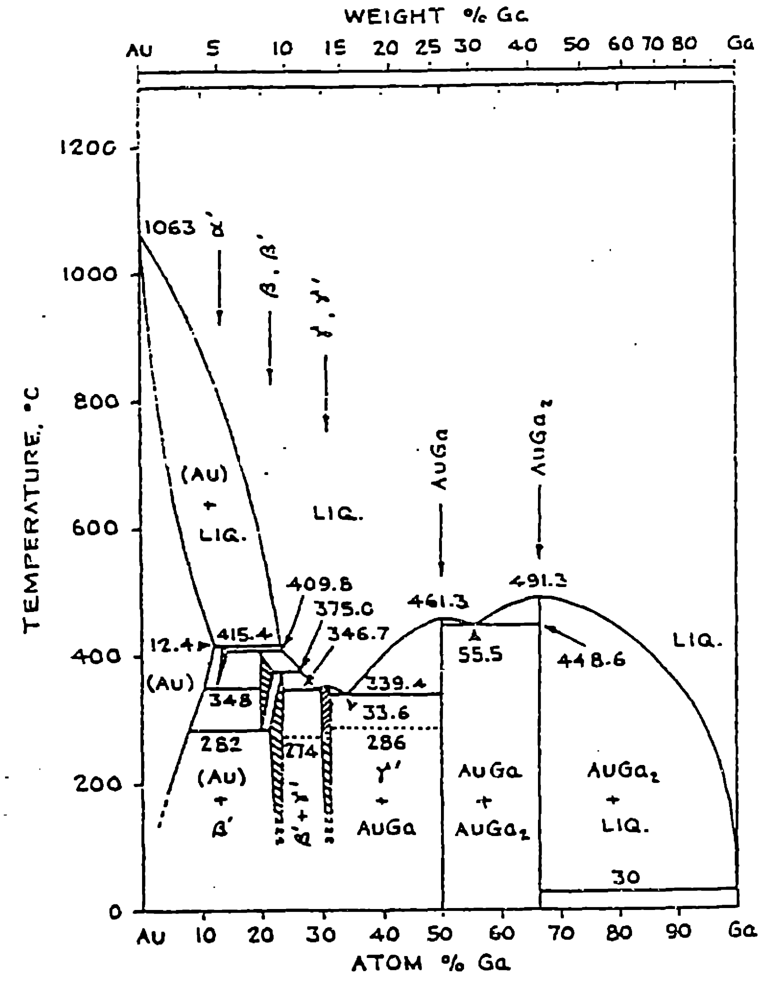

Figure 6.8: Phase diagram for Au-Ga. From [28].

6.4 Conclusion

We have demonstrated the first ion induced deposition of gold. The deposition occurs only where the ion beam is incident. Thus it can be controlled with resolution comparable to the beam diameter. The beam diameter in our case is 0.4 μm but 0.05 μm is possible in more advanced focused ion beam machines. The dependence of yield (atoms deposited/ incident ion) on scan rate has been measured. A yield of 5 atoms/ion is observed for rapid scans. The resistivity of the gold is found to be about 2 orders of magnitude higher than that of bulk gold. This deposition technique is potentially useful in the repair of x-ray lithography masks or the local rewiring of integrated circuits.

The work described is but a beginning. Much work is yet to be done in the development of focused ion beams and their applications.

6.4.1 Improving yield

As the yield change due to inadvertant pressure variations showed (sect.5.4), yield *is* a function of gas pressure. The gas pressure at the surface is estimated to be .1-.4 mtorr with the present gas feed system. This is three orders of magnitude lower than the vapor pressure of acac, so there is a considerable range of pressures still left to be explored. If yield can be improved by one order of magnitude, then it might become feasible to use this process in the repair of x-ray masks.

6.4.2 Improving conductivity

The resistivity of the films tested ($4\text{-}10\times 10^{-4}\Omega-\text{cm}$) was equivalent to that of polycrystalline silicon, a material that is often used as a conductor in integrated circuits. However, it would be preferable to have a material of as low resistivity as possible, to allow the use of this process in any situation requiring the precise placement of a conductor. Annealing of the gold films was tried only once, and no resistivity measurements were possible after the anneal (due to loss of continuity), but it seems probable that some improvement in conductivity will result if the temperature is kept below 400°C.

Bibliography

[1] E. K. Broadbent and C. L. Ramiller, *J. Electrochem. Soc.*, 131, 1427 (1984)

[2] D. J. Ehrlich, R. M. Osgood, and T. F. Deutsch, *J. Vac. Sci. Technol.*, 21, 23 (1982)

[3] S. Matsui and K. Mori, *Jpn. J. of Appl. Phys.*, 23, L706 (1984)

[4] K. Gamo, N. Takakura, N. Samoto, R. Shimizu, and S. Namba, *Jpn. J. of Appl. Phys.*, 23 L293 (1984)

[5] S. K. Ghandi, *VLSI Fab. Princ.*, Wiley (New York) 1983 pp.448-463

[6] T. F. Deutsch and D. D. Rathman, *Appl. Phys. Lett.*, 45, 623 (1984)

[7] R. S. Robinson and S. M. Rossnagel, in *Ion Bombardment Modification of Surfaces: Fundamentals and Applications*, ed. O. Auciello and R. Kelly, Elsevier (New York) 1984 pp.239-322

[8] *VLSI Technology*, ed. S. M. Sze, McGraw-Hill (New York) pp. 267-301 (1983)

[9] N. W. Parker, W. P. Robinson, and J. M. Snyder, *SPIE*, 632 76 (1986)

[10] D. K. Atwood, G. J. Fisanick, W. A. Johnson, and A. Wagner, *SPIE*, 471, 127 (1984)

[11] N. K. Kang and L. W. Swanson, *Appl. Phys. A*, 30, 95 (1983)

[12] J. Orloff and P. Sudraud, *Microelectronic Engineering*, 3, 161 (1985)

[13] J. I. Raffel, A. H. Anderson, G. H. Chapman, K. H. Konkle, B. Mathur, A. M. Soares, and P. W. Wyatt, *IEEE Transactions on Electron Devices*, ED-32, 479 (1985)

[14] Product literature, IBT, Beverly, MA

[15] A. Wagner, *Solid State Technology*, 97, May 1983

[16] H. C. Kaufmann, W. B. Thompson, and G. J. Dunn, *SPIE,* 632, (1986)

[17] H. Lezec, private communication

[18] J. P. Ducommum, M. Cantagrel, and M. Moulin, *J. Mat. Sci.,* 10, 52 (1975)

[19] C. M. Horwitz, *Rev. Sci. Instrum.,* 50, 652 (1979)

[20] F. P. Brown and A. DiNardo, *J. Appl. Phys.,* 17, 802 (1946)

[21] R. R. Kunz and T. M. Mayer, in *Proc. Int. Sym. on Electron, Ion, and Photon Beams,* in press (1986)

[22] *VLSI Technology,* ed. S. M. Sze, McGraw-Hill (New York) pp. 219-264 (1983)

[23] W. L. Brown, in *Beam-Solid Interactions and Phase Transformations,* ed. H. Kurz, G. L. Olson, and J. M. Poate, Materials Res. Soc. Symposia Proceedings, p. 53 (1986)

[24] I. S. Sokolnikoff and R. M. Redheffer, *Mathematics of Physics and Modern Engineering,* McGraw-Hill (New York) 1966

[25] M. Komuro, H. Hiroshima, H. Tanoue, and T. Kanayama, *J. Vac. Sci. Technol. B,* 1, 985 (1983)

[26] B. Smith, *Ion Implantation Range Data for Silicon and Germanium Device Technologies,* Research Studies Press Inc. (Forest Grove, OR) 1977

[27] O. Michikami and Y. Yamaguchi, *Jpn. J. Appl. Phys.,* 10, 660 (1971)

[28] C. J. Cooke and W. Hume-Rothery, *JLCM,* 17, 42 (1966)